

1 **Axially decoupled photo-stimulation and two photon readout**
2 **(ADePT) for mapping functional connectivity of neural circuits**

3

4 Matthew Koh^{1,2,#}, Francesca Anselmi^{2,#}, Sanjeev K. Kaushalya^{2,#}, Diego E. Hernandez², Walter
5 Germán Bast², Pablo S. Villar², Honggoo Chae², Martin B. Davis², Sadhu Sai Teja², Zhe Qu³,
6 Viviana Gradinaru³, Priyanka Gupta^{2,§}, Arkarup Banerjee^{1,2,§} & Dinu F. Albeanu^{1,2,§}

7

8 1. CSHL School for Biological Sciences

9 2. Cold Spring Harbor Laboratory, Cold Spring Harbor, NY, 11724, USA

10 3. California Institute of Technology, Pasadena, CA, 91125

11

12 # - equal contribution

13

14 § - Correspondence to: albeanu@cshl.edu; banerjee@cshl.edu; pgupta@cshl.edu

15

16

17

18 **Key words:** *patterned photo-stimulation, digital micro-mirror device, holographic diffuser, two*
19 *photon microscopy, all-optical physiology, 3-D functional connectivity mapping, olfactory bulb,*
20 *sister mitral/tufted cells, short axon cells*

21

22

23 **Abstract**

24 All optical physiology *in vivo* provides a conduit for investigating the function of neural circuits
25 in 3-D. Here, we report a new strategy for flexible, axially-decoupled photo-stimulation and two
26 photon readout (*ADePT*) of neuronal activity. To achieve axially-contained widefield optogenetic
27 patterned stimulation, we couple a digital micro-mirror device illuminated by a solid-state laser
28 with a motorized holographic diffuser. In parallel, we use multiphoton imaging of neural activity
29 across different *z*-planes. We use *ADePT* to analyze the excitatory and inhibitory functional
30 connectivity of the mouse early olfactory system. Specifically, we control the activity of individual
31 input glomeruli on the olfactory bulb surface, and map the ensuing responses of output mitral and
32 tufted cell bodies in deeper layers. This approach identifies cohorts of *sister* mitral and tufted cells,
33 whose firing is driven by the same parent glomerulus, and also reveals their differential inhibition
34 by other glomeruli. In addition, selective optogenetic activation of glomerular
35 GABAergic/dopaminergic (DAT+) interneurons triggers dense, but spatially heterogeneous
36 suppression of mitral and tufted cell baseline activity and odor responses, further demonstrating
37 specificity in the inhibitory olfactory bulb connectivity. In summary, *ADePT* enables high-
38 throughput functional connectivity mapping in optically accessible brain regions.

39

40

41

42

43

44

45

46 **Introduction**

47 Manipulating select neural circuit elements is critical for understanding the circuit mechanisms
48 underlying brain computation, especially when coupled with activity monitoring and behavioral
49 analysis. In recent years, optogenetic control of specific cell-types has been widely adopted as a
50 method of choice¹⁻⁵, and various combinations of optical imaging and spatial light patterning
51 techniques⁶⁻¹⁹ have achieved concurrent stimulation and activity recording, typically in the same
52 optical z-plane. This is primarily constrained by the microscope anatomy, as the photo-stimulation
53 and imaging light paths converge onto the sample through a shared microscope objective which
54 focuses both the stimulation and imaging light patterns in its fixed focal plane. Neuronal circuits
55 are however distributed in 3-D and investigating the functional connectivity of such neural circuits
56 requires flexible control and readout of neural activity in independent optical planes (e.g.
57 stimulating layer 1 dendrites and monitoring neuronal activity in layers 5, **Fig. 1a**).

58
59 Several strategies have been developed over the past two decades to target multiple optical z-
60 planes simultaneously, or in quick succession. These range from dual scanning head
61 implementations¹⁹ to using tunable focusing elements (e.g. electrically-tunable lenses, ETL)
62 whose focal length can be dynamically controlled²⁰⁻²², acousto-optic deflector (AOD)-based
63 arbitrary access imaging systems^{14,23-28} and digital holography^{8,9,13,27,29-33}. These methods have
64 varying trade-offs, and to date, monitoring and photo-activating neurons in three dimensions
65 remains challenging. When choosing an adequate photo-stimulation and imaging approach,
66 several aspects are worth considering: the required spatial resolution in 3-D (stimulating individual
67 cell bodies versus extended patches of tissue), the size of the field of stimulation, the axial
68 separation between the stimulation and imaging planes (relative locations of the input-output nodes

69 of the circuit), the cost and simplicity of implementation and its robustness. Early scanning-based
70 methods enabled photo-stimulation over large fields of view (FOVs), but conferred poor axial
71 resolution^{34,35}, potentially leading to off target photo-activation in 3-D. In contrast, modern
72 methods achieved flexible and precise 3-D confinement of photo-stimulation using AOD-based
73 approaches, or digital holography in combination with temporal focusing^{8,9,13,27-33}. AOD-based
74 and holographic control of activity, however, can be technically challenging and cost-prohibitive,
75 and the size of the field of photo-stimulation is limited by steep power requirements. Axial
76 decoupling between the stimulation and imaging planes has also been achieved by simpler methods
77 such as using ETLs, but these implementations are constrained by spherical aberrations which
78 deteriorate the point spread function and limit the size of the field of stimulation.

79
80 Here we introduce *ADePT* (Axially Decoupled Photo-stimulation and Two-Photon readout), an
81 easy implementable, cost-effective and high-throughput technique that combines one-photon
82 widefield patterned illumination with multiphoton imaging in axially decoupled planes (**Fig. 1b**).
83 Our approach enables precise axially-confined photo-stimulation, with arbitrarily shaped light
84 patterns, across an extended region on the brain surface, while imaging neuronal activity in other
85 optically accessible z-planes of choice. We use a digital micro-mirror device (DMD)^{17,36-46} to
86 impose customizable 2-D spatial patterns onto a Gaussian laser beam that are subsequently
87 optically relayed onto the sample. Due to the coherent nature of the illumination source (laser), the
88 spatial patterning is maintained throughout the optical path between the DMD chip and the sample
89 (infinite focus). Placing a (holographic) diffuser in the optical path breaks the coherence and
90 disrupts this infinite focus. The desired 2-D pattern comes into focus only in an axially confined
91 optical-plane in the sample that is conjugate to the diffuser. To flexibly target photo-stimulation

92 across different depths in the sample, independent of the multiphoton imaging plane (objective's
93 focal plane), we simply translate the diffuser along the optical path using a motorized stage. Akin
94 to remote focusing imaging approaches^{16,20,47–52}, translating the diffuser displaces the optical z-
95 plane within the sample where the stimulation pattern is in focus independent of the objective's
96 focal plane (**Fig. 1c**). In our implementation, we report ~20 μm lateral (17.1 μm x-y-FWHM) and
97 ~40 μm axial (36.3 μm z-FWHM) resolution of the patterned photo-stimulation across a 1.2 x 1.5
98 mm field of stimulation (20X, 1.0 NA, Olympus objective). We calibrated this method across up
99 to 500 μm axial displacement between the photo-stimulation plane and the focal plane of the
100 objective. Note that these parameters are not strictly rigid, and *ADePT* can accommodate many
101 different operating configurations depending upon the specific biological application.

102

103 We subsequently assessed the effectiveness of *ADePT* for investigating the logic of circuit
104 connectivity by leveraging the 3-D spatial layout of the mouse olfactory bulb (OB)^{53,54}. In the OB,
105 the input nodes called glomeruli (balls of neuropil sorted by odorant receptor identity) and the
106 principal output neurons (mitral and tufted cells) are separated by approximately two hundred
107 microns in depth. We investigated the excitatory and inhibitory logic of this early olfactory circuit
108 by photo-stimulating either the glomeruli or local inhibitory interneurons while monitoring
109 responses of mitral/tufted cells (MT cells). We found that *sister* OB output neurons^{36,55–61} – those
110 that receive primary input from the *same* 'parent' glomerulus – differ substantially in their lateral
111 inhibitory connectivity with other glomeruli with the OB network, potentially explaining their non-
112 redundant responses to odors³⁶. Further, we found that local GABAergic/dopaminergic
113 interneurons^{42,43,62–66} associated with different glomeruli provide dense but selective inhibition to
114 regulate odor responses of OB output neurons. In summary, *ADePT* is readily-deployable and well-

115 suited for high-throughput mapping of both excitatory and inhibitory functional connectivity in
116 optically accessible brain regions.

117

118 **Results**

119 **Design of the axially decoupled patterned photo-stimulation and imaging setup**

120 We couple a custom laser scanning two photon microscope (Methods) with a modular add-on for
121 axially-contained widefield (one-photon) patterned photo-stimulation (**Fig. 1b**). Patterned photo-
122 stimulation is achieved using a digital micro-mirror device (VX4100 DMD, 0.7" XGA VIS 1024
123 x 768 pixels, 13.68 μm micro-mirror pitch, Vialux) illuminated by a solid-state CW laser
124 (Sapphire, 488 nm, 200 mW, Coherent). The photo-stimulation and two-photon excitation paths
125 are combined using a dichroic mirror (680dcxr, 50 mm diameter, Chroma) placed above the
126 objective (20X, 1.0 NA, Olympus). A diffuser mounted on a motorized translation stage enables
127 flexible control of the axial location of the photo-stimulation plane in the sample (**Figs. 1a-c**).
128 Without the diffuser, the photo-stimulation 2-D pattern is in focus throughout the optical path as
129 pencils of coherent light (**Fig. 1c, Top**). By placing the diffuser in the optical path, the coherence
130 of the beam is disrupted and the 2-D spatial pattern imposed by the DMD is accurately
131 reconstructed in the sample only in a thin (axially-contained) image plane. This image plane is
132 optically conjugated with both the diffuser and the DMD chip. In the default 4f configuration, the
133 DMD pattern thus comes into focus in the focal plane of the objective such that the photo-
134 stimulation and multiphoton imaging planes overlap axially (**Fig. 1c, Middle**). Importantly,
135 translating the diffuser along the optical path causes its conjugate image plane in the sample to
136 move as well, therefore axially decoupling the photo-stimulation plane from the focal (sample)
137 plane of the imaging objective (**Figs. 1b-c, Bottom, S1a-b**).

138 Introducing a diffuser in the optical path has the added benefit of improving the axial confinement
 139 of the photo-stimulation pattern. The diffuser breaks the coherence of the DMD-modulated laser
 140 pattern, dispersing light across a solid angle (Methods). As the photo-stimulation pattern in the
 141 sample plane is a conjugate image of the diffuser, it is expected to be restricted to a thin optical z-
 142 plane and its axial extent to scale linearly with the lateral (x-y) spot size^{6,12,67}. Note that this differs
 143 from the focusing regime of a Gaussian laser beam where the axial extent of the focal spot
 144 increases quadratically with the lateral extent of the spot. In *ADePT*, the axial confinement of the
 145 photo-stimulation pattern depends directly on the available light angles emerging from the diffuser
 146 (effective numerical aperture): the wider the cone of angles, the tighter the axial confinement
 147 (higher axial resolution) albeit with increased loss of excitation light.

Figure 1

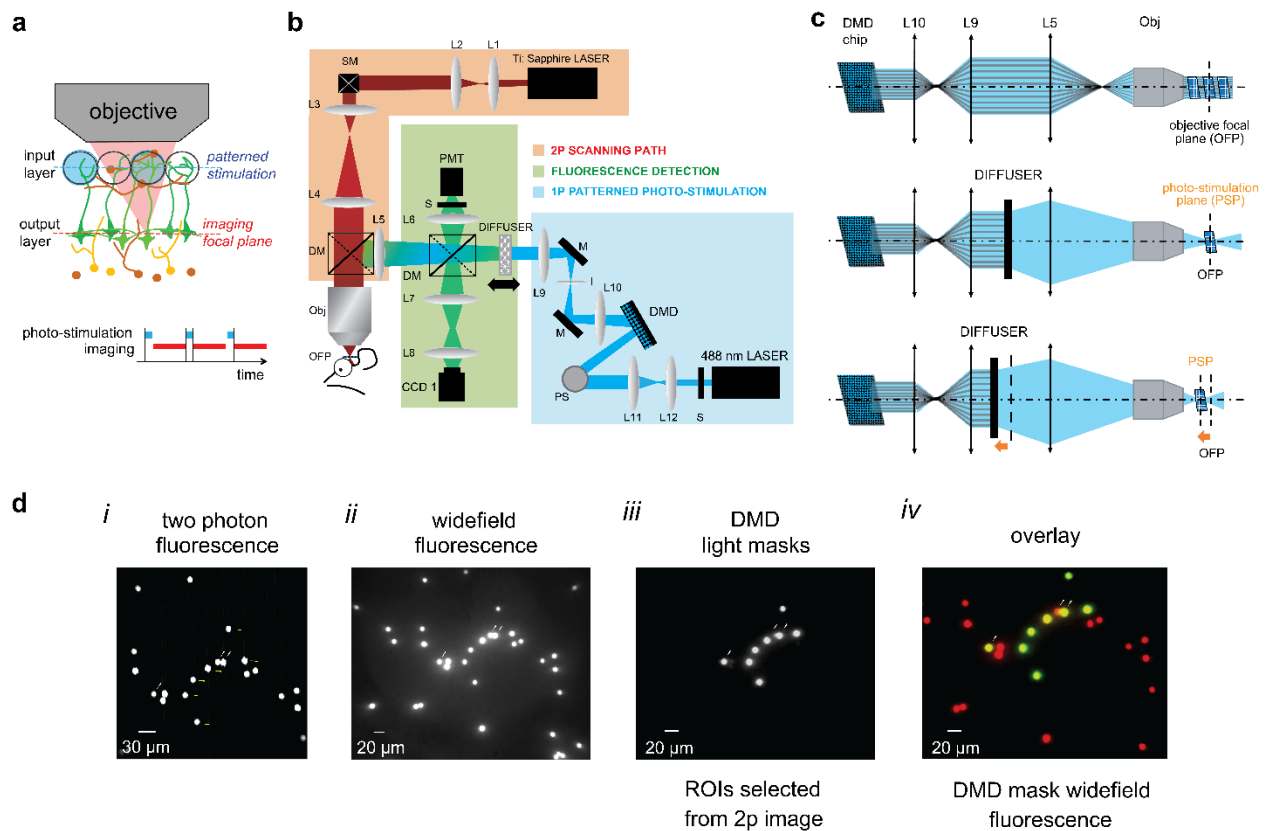


Figure 1: Axially decoupled patterned photo-stimulation and multiphoton imaging. (a) (Top) Cartoon schematics of functional connectivity mapping of a neural circuit (e.g. olfactory bulb);

photo-stimulation (2-D light mask from a digital micro-mirror device illuminated with a solid-state CW laser) and two photon imaging are confined to different optical z-planes that can be flexibly and independently adjusted by translating the diffuser and respectively the primary objective; (Bottom) Alternating (strobing) between photo-stimulation and imaging periods. Each red bar represents a single frame of multiphoton imaging. Photo-stimulation and imaging periods are interleaved. (b) Microscope schematics. DM, dichroic mirrors. DMD, digital micro-mirror device. I, iris diaphragm. L1-L12, lenses. O, primary objective. PMT, photomultiplier tube. PS, periscope. S, shutter. SM, scan mirrors. (c) (Top) Illustration of using a movable diffuser to decouple the patterned photo-stimulation and multiphoton imaging planes. The diffuser is imaged into the sample, in a 4f lens configuration; translating the diffuser along the optical path causes the corresponding projection plane to shift axially. OFP, objective focal plane. PSP, photo-stimulation plane. (d) DMD chip-to-CCD camera-to-2p microscope registration. (i) two photon micrograph of 10 μm fluorescence microbeads; arrows mark two microbeads, part of the larger DMD-modulated projection target pattern (8 microbeads), which were taken as fiduciary points; (ii) widefield fluorescence image (full field illumination) of a larger field of view including the target microbeads; (iii) ROIs selected from the 2p image were used to generate DMD-chip light masks; these were further projected at the primary objective focal plane and imaged using the primary CCD camera (CCD 1); (iv) overlay of DMD-generated photo-stimulation masks and widefield fluorescence image of 10 μm microbeads from (ii); note that fluorescence is restricted to the microbeads targeted by the DMD photo-stimulation masks with minimal spillover to adjacent (off-target) microbeads (see fiduciary marks).

148 We registered the DMD field of stimulation (DMD pixel size = 2.4 μm at the sample, **Fig. 1d**) to
149 the primary CCD camera image (CCD1 pixel size = 1.1 μm at sample; CCD 1300-QF, Vosskuhler)
150 and the multiphoton field of imaging into a common reference frame (Methods). We verified that
151 the targeting of DMD-modulated spatial light patterns was precise (< 5 μm error, note that
152 fluorescence is restricted to the microbeads targeted by the DMD photo-stimulation masks with
153 minimal spillover to adjacent, off-target microbeads, **Fig. 1d, 2b, S1d**). To ensure flat photo-
154 stimulation probability across the field, we measured and further corrected light power
155 inhomogeneities arising due to the Gaussian profile of the photo-stimulation laser beam and
156 aberrations along the optical path (**Fig. S1e**). In control experiments (no fluorescent sample), we
157 observed unwanted phosphorescence upon photo-stimulation, depending on the lens material
158 (BK7 vs. fused silica). Consequently, we compared different objective and lens combinations and

159 chose the primary objective (20X, 1.0 NA, Olympus) and collection tube lens (L5; 100 mm FL,
160 fused-silica, LA4545-A, Thorlabs) such as to minimize these artifacts (**Fig. S1f**, Methods).

161

162 **Lateral and axial resolution of photo-stimulation**

163 To determine the lateral and axial resolution of photo-stimulation setup, we projected light spots
164 of increasing nominal diameters onto a glass coverslip spin-coated with 1 μ m thick rhodamine B
165 layer (**Figs. 2,3**). We measured the resulting fluorescence signals by imaging the rhodamine-coated
166 coverslip from below with an inverted (secondary) microscope. The secondary microscope was
167 set up so as to be confocal with the primary microscope objective (**Figs. 2a-c, 3a**)⁶. Each spot was
168 sampled through the fluorescent coverslip by moving the primary objective up or down in steps of
169 1-2 μ m. We used the images acquired by the primary (CCD1) and secondary (CCD2) cameras
170 (**Fig. 3a**; CCD1300QF, Vosskuhler) to obtain the lateral (x-y) and axial (z) extent of the light
171 intensity profile at full width half maximum (FWHM, **Figs. 2b-c, S2a-b**). Using this strategy, the
172 smallest resolvable photo-stimulation spot we achieved was \sim 20 μ m in lateral diameter (17.1 μ m
173 FWHM, **Figs. 2b, S2a-b**). Below this size, decreasing the nominal spot size did not change the
174 measured x-y-FWHM of the spot, potentially due to light scattering from the extended spot, light
175 loss and imperfections in the setup's optical transfer function.

176

177 We further investigated the effect of the choice of diffuser on the z-FWHM for projected light
178 spots of different sizes. As reported previously for light patterning techniques such as digital
179 holography^{6,12,67}, we observed a linear dependence between the axial and lateral extent of the light
180 patterns projected (z-FWHM vs. x-y-FWHM of photo-stimulation spots, **Fig. 2c**). As expected,
181 the ratio between the axial vs. lateral resolution was inversely proportional to the diffuser

182 divergence angle (slope = 1.52 when using a *grit ground* diffuser, #38-786 vs. 1.62 for a 10°
183 *holographic* diffuser, #48-506 vs. 2.12 for a 5° *holographic* diffuser, #55-849, Edmund Optics,
184 **Fig. 2c**). In other words, the axial spread of the projected light pattern increased as the diverging
185 angle of the *holographic* diffuser got narrower (lower NA). To minimize excitation light loss while
186 maintaining ~40 μm axial resolution, we settled on a 5° *holographic* diffuser, a diffractive optical
187 element designed to limit the spread of transmitted light to a specified solid angle (e.g., 5°, #55-
188 849, Edmund Optics, **Fig. 2c**). Using a 5° *holographic* diffuser only slightly under-filled the
189 angular aperture of the primary objective and did not affect the lateral resolution of the system.
190 Using a 10° *holographic* diffuser, or a *grit ground* diffuser would further increase the axial
191 specificity (~30 μm) at the expense of light loss.

Figure 2

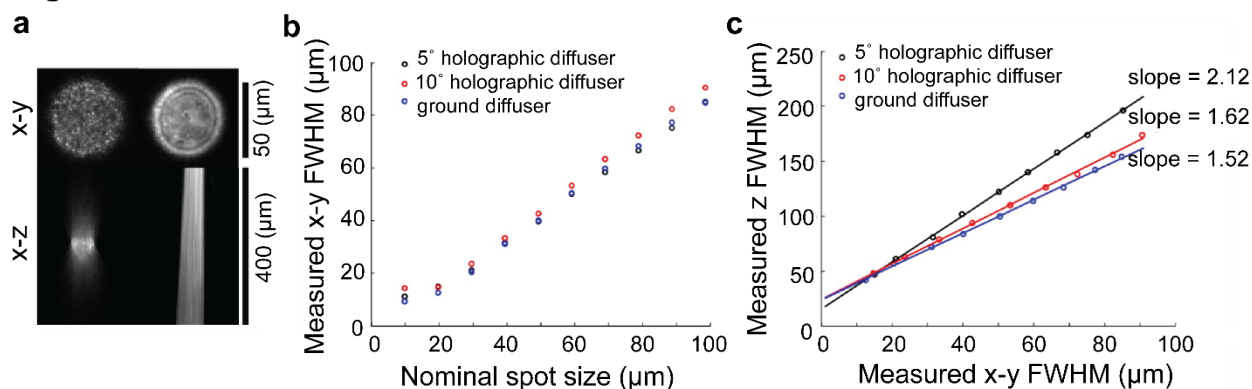


Figure 2. Axial confinement and resolution of the patterned stimulation and multiphoton imaging setup. (a) Axial confinement of light intensity of a 2-D projection pattern using a holographic diffuser conjugated to the focal plane of the principal objective (Left) vs. same optical configuration without a diffuser (Right); spot diameter = 50 μm. (b) Measured spot x-y FWHM versus expected nominal spot size calculated by multiplying the pattern size in pixels by the expected size of a pixel given the DMD chip and the optical magnification of the system. Circular spots of different sizes (10-100 μm in diameter) were projected on a glass slide coated with a 1 μm thin layer of rhodamine B. (c) Measured axial (z) FWHM versus lateral (x-y) FWHM of the projected spots from (b) for three different types of diffusers; black circles = 5° holographic diffuser; red circles = 10° holographic diffuser; blue circles = grit ground diffuser.

192 **Decoupling imaging and photo-stimulation across different z-planes**

193 To flexibly manipulate the relative positioning of the photo-stimulation plane with respect to the
194 multiphoton imaging plane, we physically translate the diffuser on a motorized stage (**Fig. 1b**).
195 Theoretically, we expect a linear relationship between the axial displacement of the objective and
196 the corresponding compensatory displacement of the diffuser that is proportional to the square of
197 the magnification of the optical system (Eqs. 1-5, Methods). To verify and experimentally calibrate
198 the decoupling of photo-stimulation and imaging planes across a range of depths in our setup, we
199 projected a checker-board light pattern on a fluorescent coverslip coated with a $\sim 1 \mu\text{m}$ thin layer
200 of rhodamine B. We imaged the resulting fluorescence through both the primary microscope and
201 a secondary inverted widefield microscope placed below (**Fig. 3a**)⁶. In the default configuration,
202 the diffuser is conjugate to the sample (objective focal plane), the secondary objective is confocal
203 with the primary objective, and the rhodamine coverslip is placed in their shared focal plane (also
204 the sample plane). The photo-stimulated pattern thus appears in focus on both CCD1 (primary
205 objective) and CCD2 (secondary objective). As we lowered the primary objective, as one would
206 to image deeper structures in a sample, the projected pattern also moved lower (below the
207 coverslip). This can be observed as a blurred image of the photo-stimulation pattern on CCD2 as
208 its imaging plane is still conjugate to the rhodamine coverslip. We determined the extent of the
209 diffuser displacement necessary to re-focus the projected pattern back onto the original plane of
210 interest in the sample (the rhodamine coverslip) by translating the diffuser away from the objective
211 until a sharp image of the checker-board reappeared on CCD2 (**Fig. 3a**). Moving down the primary
212 objective by incremental amounts ($100 \mu\text{m}$) and monitoring the required diffuser displacement via
213 the secondary microscope, we obtained a calibration curve, describing the effective decoupling of

214 the imaging and photo-stimulation planes up to 500 μm (i.e. spanning the 50 mm range of a
 215 Newport 433 translation stage we used to mount the diffuser, Methods, **Fig. 3b**).

216 As the photo-stimulation pattern was moved away from the focal plane of the objective, we
 217 measured a slight increase in lateral (<10%) and axial extent (<20%, **Fig. 3c**), which we further
 218 accounted for by applying corrections in the control software (Methods). Over the axial
 219 displacement interval sampled, we observed a linear relationship between translating the objective
 220 axially and the compensatory displacement of the diffuser required to bring the pattern back into
 221 focus, proportional to the square of the effective optical magnification in our setup (theoretical vs.
 222 effective magnification $\sim 11.1 \text{ X}$ vs. $\sim 9.3 \text{ X}$, **Fig. 3b**, Methods).

Figure 3

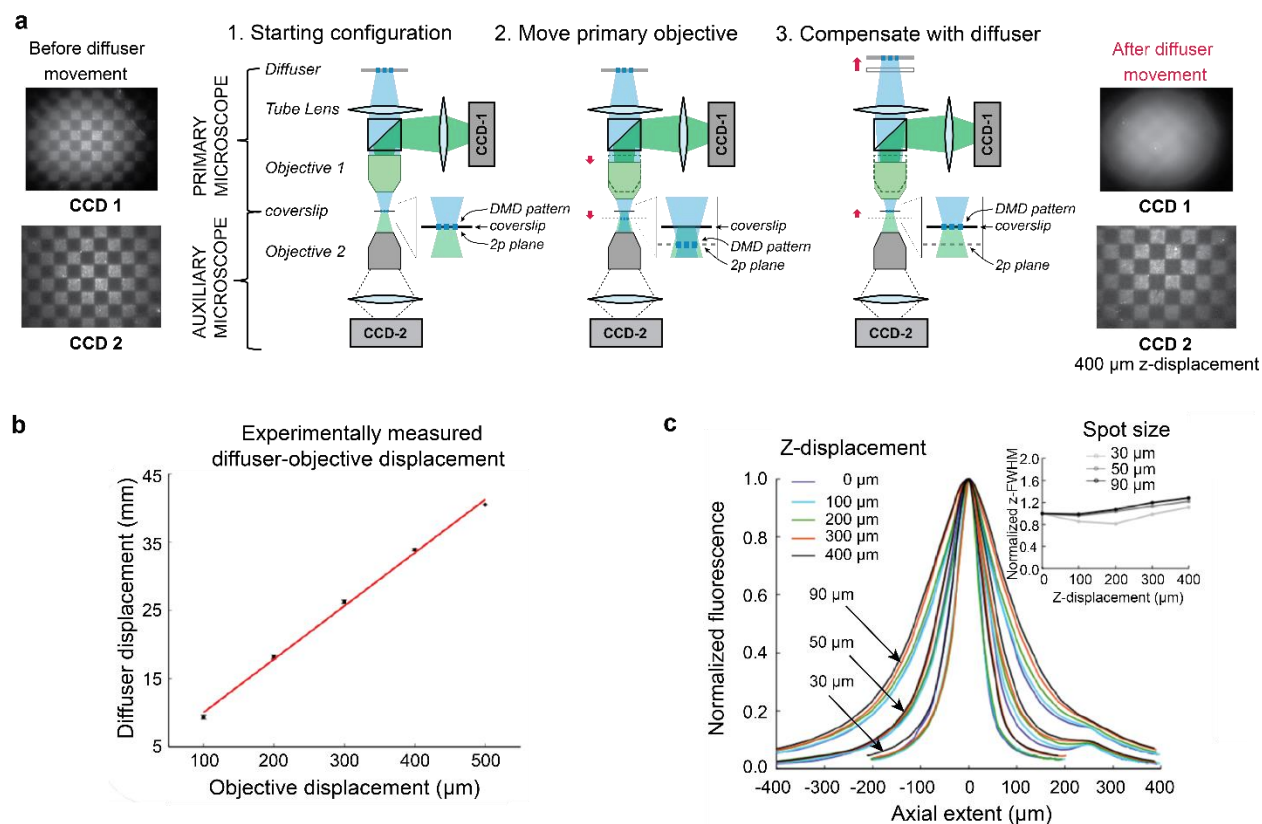


Figure 3. Decoupling the photo-stimulation and imaging z-planes using a translatable diffuser. (a) Schematic cartoon describing using of the primary and secondary (auxiliary) microscopes to calibrate the decoupling of the photo-stimulation and optical-readout planes. A thin (1 μm) rhodamine B fluorescent coverslip sample is placed in the focal plane of both primary and

secondary microscope objectives, where a checker-board pattern is projected using the DMD-chip (Step 1). Lowering the primary objective by a given amount translates the pattern axially below the focal plane of the secondary objective (which remained stationary), and produces a blurred image of the checker-board pattern on the secondary (CCD2) camera (Step 2). The projected light pattern is brought back into focus on CCD2 by compensating with translating the diffuser along the optical path (i.e. moving the diffuser away from the back-aperture of the primary objective, which defocuses the image on the primary (CCD1) camera (Step 3). (b) Measured calibration curve of diffuser translation required to shift photo-stimulation plane by a given amount with respect to the focal plane of the objective. Each point represents Mean \pm SEM across several months, indicating the robustness of the setup and linear relationship between objective and compensatory diffuser displacements for the range of photo-stimulation and imaging plane decoupling sampled (500 μm). (c) Normalized axial light intensity profile of spots. Measurements for spots of three different diameters (30, 50 and 90 μm), indicated by the three clusters of color traces. Each line color represents a different diffuser offset, expressed as degree of axial displacement between the photo-stimulation and focal plane of the primary objective in 100 μm steps (0 to 400 μm). (Inset) Measured change in axial (z) FWHM of the light profiles in c. as a function of axial displacement between photo-stimulation and imaging planes relative to no-offset (z-overlapping) condition, which we further accounted for by applying corrections in the control software.

223 **Quantifying photo-stimulation pattern propagation through brain tissue**

224 One-photon patterned stimulation is constrained to surface applications because of limited
225 penetration of shorter wavelengths into tissue due to scattering. To characterize the propagation of
226 DMD-generated light patterns through brain slices of different thickness^{68,69}, we placed fixed
227 olfactory bulb slices (Methods) atop a fluorescent coverslip, and recorded images of the projected
228 patterns from underneath with the auxiliary microscope. To reduce the effect of variability in
229 slicing angle and local neuronal architecture, we acquired images at two axial locations in each
230 slice (Methods). Patterns remained distinct in slices up to ~ 150 μm thick (**Figs. S2c-f**), albeit
231 substantial fluorescence loss (**Fig. S2f**). We note that using the diffuser, besides confining the axial
232 spread of photo-stimulation, also increases the homogeneity of the projected light patterns in
233 scattering media (**Figs. S2f-g**). Without the diffuser in the optical path, patterns appeared speckled:
234 standard deviation of pixel intensities within the pattern was higher compared to same thickness
235 samples with the diffuser in place (**Figs. S2e-g**). This effect can be explained intuitively by taking

236 a ray-tracing point of view on image formation. With the diffuser in the optical path, due to angular
237 dispersion, light emitted from a single point in the pattern travels along more paths through the
238 tissue compared to the no-diffuser condition to reach at a given camera pixel (**Fig. S2e**). As such,
239 using the diffuser increases homogeneity in light intensity across the field of stimulation, as this
240 configuration is less sensitive to variations in scattering from local structure in the tissue.

241

242 **Mapping functional connectivity in the intact brain**

243 *ADePT* combines precise, patterned optogenetic stimulation of the brain with high-resolution
244 monitoring of resultant neuronal activity. This method is ideal for investigating the logic of
245 functional connectivity in layered neuronal circuits where input and output circuit elements do not
246 necessarily lie in the same plane. In addition, our one-photon DMD based implementation is
247 particularly well-suited for understanding information flow in areas where sensory stimuli evoke
248 structured spatiotemporal patterns of activity that extend over several 10s of microns (e.g.
249 glomeruli in the olfactory, whisker barrels in barrel cortex, etc.). As a proof of principle, we used
250 *ADePT* to investigate the role of different local inhibitory and excitatory connections in shaping
251 the output of the mouse olfactory bulb. Briefly, in the OB, the input nodes called glomeruli (balls
252 of neuropil sorted by odorant receptor identity) and the cell bodies of the principal output neurons
253 (mitral and tufted cells) are separated by a couple hundred micrometers in depth^{53,54}. Individual
254 odors activate distinct spatial-temporal combinations of glomeruli. This odor-evoked activity is
255 heavily reformatted within the OB by numerous excitatory and inhibitory interneurons and relayed
256 to other brain areas in the form of activity patterns of the mitral/tufted cells. To date, understanding
257 the OB computations has been challenging due to constraints in precisely and flexibly controlling
258 the activity of individual input nodes (glomeruli) using traditional odor stimuli. Using *ADePT* we

259 can bypass these constraints by direct photo-stimulation while simultaneously monitoring the OB
260 outputs at high throughput and cellular resolution.

261

262 **Application 1: Mapping glomerular receptive fields of sister mitral/tufted cells**

263 We used *ADePT* to first identify cohorts of *sister* output cells in the OB – mitral and tufted cells
264 that receive excitatory input from the same *parent* glomerulus^{36,55–61} – and then assess whether
265 they integrate lateral inputs from different sets of glomeruli in the OB. Indeed, *sister* mitral and
266 tufted cells extend multiple secondary (lateral) dendrites, which may each contact different sets of
267 inhibitory interneurons^{36,55,56,70}. Previous work has shown that while *sister* cells are generally
268 responsive to the same set of odors, they are not redundant in their odor responses: pairs of *sister*
269 cells are as different as pairs of *non-sisters* in their response time with respect to inhalation
270 onset^{36,55}. A potential mechanism for temporal differences in the odor-evoked responses of *sister*
271 cells is differential inhibitory inputs from other glomeruli in the OB. However, to date, mapping
272 glomerular receptive fields of individual mitral/tufted cells has been difficult given technical
273 limitations in precise control of single-glomerulus activity in conjunction with monitoring
274 responses at a high-enough yield to identify and further compare cohorts of *sister* mitral/tufted
275 cells. Using *ADePT* enabled us to bypass the constraints imposed by odor stimulation and directly
276 photo-stimulate individual glomeruli on the OB surface. In parallel, it enabled monitoring the
277 responses of many mitral/tufted cells simultaneously at cellular resolution using multiphoton
278 calcium imaging. To this end, we used mice expressing both an opsin in the mature olfactory
279 sensory neurons (OSN), OMP-Cre x ReaChR-mCitrine⁷¹ and the genetically encoded calcium
280 indicator (GCaMP6f/s⁷²) in the mitral and tufted cells (Thy1-GCaMP6s⁷³; **Fig. S3a**, Methods).

Figure 4

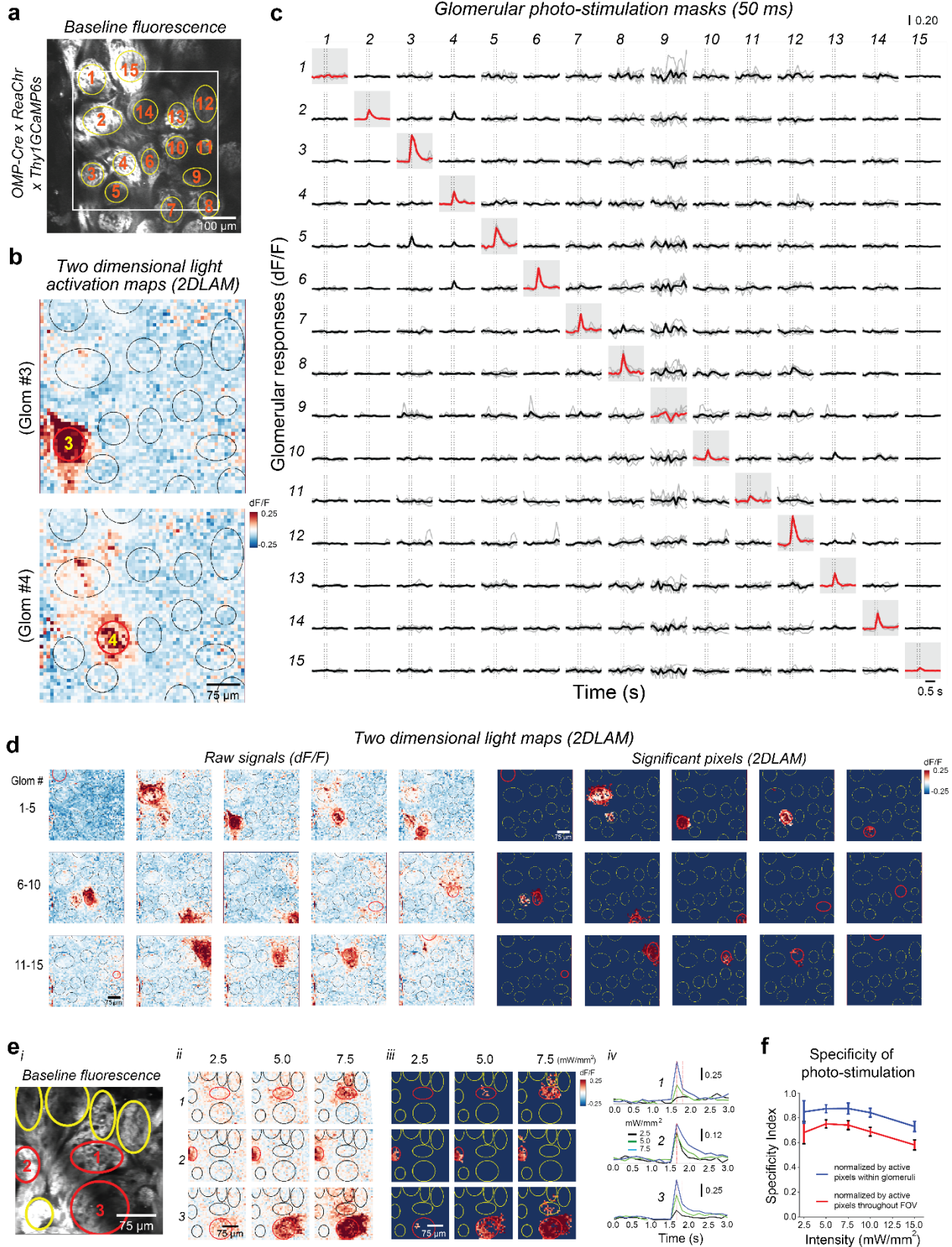


Figure 4. Targeting individual glomeruli by photo-stimulation of olfactory sensory neuron terminals and monitoring glomerular responses of sister mitral and tufted cell dendrites. (a) (i) Glomerular resting fluorescence in OMP-Cre x ReaChR-citrine x Thy1-GCaMP6s mice; (b) Fluorescence changes (two dimensional glomerular light activation maps, 2DLAMs) evoked by photo-stimulation of 2 example glomeruli (#3, #4) out of 15 glomeruli targeted in the example field of view (5.0 mW/mm^2 for 50 ms). Red ellipses mark the location and contour of the projected light masks. Color scale in heat map indicates $\Delta F/F$, comparing fluorescence after light stimulation to baseline; (c) Response matrix of fluorescence traces (individual repeats in gray, and mean signal as thicker lines) corresponding to 15 glomerular regions of interest versus the 15 (matching) glomerular light masks projected on the OB surface. Red traces mark responses of the targeted glomerulus in a given trial. (d) (Left) Fluorescence changes (two dimensional glomerular light activation maps, 2DLAMs; 5.0 mW/mm^2) evoked by photo-stimulation of the 15 glomeruli targeted in the example field of view (a). (Right) Significant 2DLAMs. Non-significant responses were thresholded to blue background. Out of 15 targeted glomeruli, 5 glomeruli were considered non-responsive, given our signal threshold criteria (Methods). Of the 10 responsive light maps, 8 showed specific responses (pertaining to the target glomerulus), and 2 light maps were not specific (responses were observed across multiple glomeruli). (e) Example target glomeruli from a different example FOV across a range of three light intensities (2.5 , 5.0 and 7.0 mW/mm^2). Projected light masks match the red ellipses in (i) and (ii). Color scale in heat map indicates $\Delta F/F$, comparing fluorescence triggered by light stimulation to baseline; (iii) Same as (ii) for statistically significant glomerular photo-stimulation responses (rectified 2DLAMs); (iv) Fluorescence traces (mean signal for each light intensity) corresponding to three regions of interest (ROI) in each heat map, whose position is indicated by red ellipses in i-iii. Different intensities are represented by different color traces (red - 2.5 mW/mm^2 , green - 5.0 mW/mm^2 , blue - 7.5 mW/mm^2). (f) Specificity of glomerular responses across light intensity. Blue trace: responsive pixels within the target glomerulus normalized by all responsive pixels located within glomerular boundaries across the FOV. Red trace: responsive pixels within the target glomerulus normalized by all responsive pixels within the FOV, including those spanning the juxtglomerular space, surrounding glomeruli (Methods); $N=7$ mice, 21 FOVs; responsive vs. photo-stimulated glomeruli: 2.5 mW/mm^2 , 12/74; 5.0 mW/mm^2 , 48/122; 7.5 mW/mm^2 , 27/57; 10.0 mW/mm^2 , 48/98; 15.0 mW/mm^2 , 48/77.

282 We stimulated glomeruli by projecting DMD-modulated light masks on top of individual
283 glomeruli, identified based on their baseline fluorescence (Methods). We used photo-stimulation
284 spot sizes smaller ($30\text{-}50 \mu\text{m}$) than the targeted glomeruli (Avg. $\sim 75 \mu\text{m}$)^{36,74}. To assess the
285 resultant responses in the mitral/tufted cells, we strobed between stimulating OSN axon terminals
286 ($50\text{-}150 \text{ ms}$ stimulation) and monitoring calcium responses ($5\text{-}10 \text{ Hz}$ imaging rate) in either the
287 postsynaptic mitral/tufted dendritic tufts in the glomerular layer (same z-plane) or the cell-bodies
288 ($100\text{-}270 \mu\text{m}$ below the photo-stimulation plane). First, we calibrated the stimulation light intensity
289 to ensure single glomerulus specificity – photo-stimulation of OSNs only within the targeted

290 glomerulus while avoiding spurious excitation of passing-by OSN axons that terminate in
291 neighboring glomeruli. To assess the efficacy of our approach, we set the photo-stimulation and
292 multiphoton activity readout planes to overlap axially in the glomerular layer, such as to stimulate
293 the OSNs and image the resultant postsynaptic glomerular response in the dendrites of MT cells.
294 Photo-stimulation induced rapid and reliable changes in fluorescence (**Fig. 4**). For each photo-
295 stimulation mask (**Figs. 4b-e, S3b**), we constructed a two-dimensional light activation map
296 (2DLAM) at sub-glomerular resolution³⁶ (e.g. 40 x 40 grid of 7.2 μm pixels, Methods). To ensure
297 we operated in a regime of specific glomerular activation, we successively lowered the light
298 intensity until no light-triggered activity was observed in neighboring glomeruli (15-to-2 mW /
299 mm^2 , 122 glomeruli, 21 FOVs, 7 mice, **Figs. 4f, S3c**). Across mice, we identified a range of
300 intensities that on average resulted in specific and reliable activation of targeted glomeruli and
301 negligible activation of adjacent glomeruli (**Fig. 4f**).

302

303 Next, we axially decoupled the photo-stimulation and imaging z-planes to monitor light-triggered
304 responses in the cell bodies of the corresponding *daughter* M/T cells (receiving excitatory input
305 from the targeted glomeruli, and 100-270 μm deep from surface), while still photo-stimulating
306 individual glomeruli on the bulb surface (**Figs. 5a-e, S4a-f**). Photo-stimulation of individual
307 glomeruli evoked robust excitatory responses in ~19 % of the cells (162/856). The majority of
308 these responsive cells (141/162) were activated by only one unique glomerulus that we ascribed
309 as their corresponding parent glomerulus. A small proportion of cells were activated by more than
310 one glomerulus and excluded from further analysis (21/162 cells, **Fig. 5b iii**, cell 30). By
311 comparing the identity of parent glomeruli across the imaged M/T cells, we identified cohorts of
312 *sisters* as the cells that were activated by the same parent glomerulus.

Figure 5

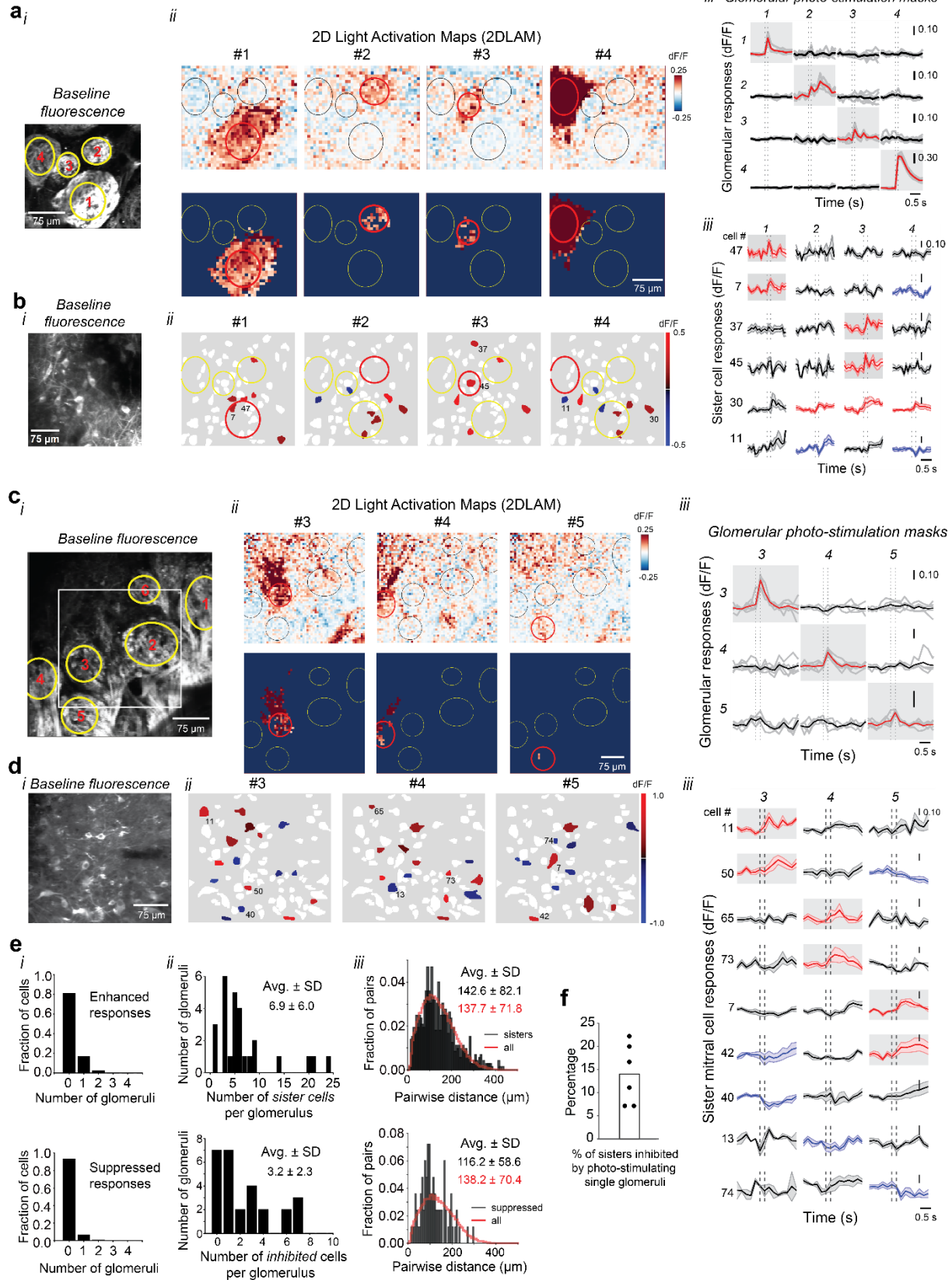


Figure 5. Identifying sister mitral and tufted cells via axially decoupled glomerular stimulation and two photon fluorescence imaging. (a-b) anaesthetized, (c-d) awake. (a) (i) Resting glomerular fluorescence (ReaChR-mCitrine and GCaMP6s); (ii) Fluorescence changes (raw, Top and significant pixels glomerular 2DLAMs, Bottom) evoked by photo-stimulation of four target glomeruli (7.5 mW/mm^2); (iii) Response matrix of fluorescence change traces (individual repeats in gray, and mean signal as thicker lines) corresponding to four glomerular regions of interest versus the four corresponding (matching) glomerular light masks projected on the OB surface. Red shaded areas mark responses of the targeted glomerulus in a given trial. (b) (i) Resting fluorescence (GCaMP6s) of mitral cell bodies at the same x-y coordinates, $210 \mu\text{m}$ below the glomerular field of view in (a); (ii) Significant cell body responses evoked by photo-stimulation of the four target glomeruli (7.5 mW/mm^2); (iii) Average fluorescence response traces corresponding to six example mitral cells in each heat map, whose positions are indicated by numbers in (ii); shaded area marks SEM. Two example pairs of sister cells (47, 7 with respect to parent glomerulus #1; and 37, 45 with respect to parent glomerulus #3) are shown. Note that cell #30 is non-specifically responding to photo-stimulation of multiple glomeruli (#2,#3,#4). In addition, glomerular photo-stimulation triggered sparse suppressed responses (e.g. cells 7,11) intermingled with the sister cells. (c) (i-iii) Same as (a) for an example awake experiment: photo-stimulation of three target glomeruli (2.5 mW/mm^2 ; 50 ms light on/trial); (iii) Response matrix of fluorescence change traces (individual repeats in gray, and mean signal as thicker lines) corresponding to three glomerular regions of interest (#3,#4,#5) versus the three (matching) glomerular light masks projected on the OB surface. Stimulation of glomeruli #1 and #2 resulted in non-specific responses. (d) (i-iii) same as (b) for an example awake experiment sampling mitral cell bodies at the same x-y coordinates, $190 \mu\text{m}$ below the glomerular field of view shown in (c); (ii) Significant cell body responses evoked by photo-stimulation of three target glomeruli (c,ii); (iii) Average fluorescence time traces corresponding to nine example mitral cells in each heat map, whose positions are indicated by numbers in (ii). Three example pairs of sister cells (11, 50 with respect to parent glomerulus #3; 65, 73 with respect to parent glomerulus #4; and 7 and 42 with respect to parent glomerulus #5) are shown. Glomerular photo-stimulation also triggered spatially distributed suppressed responses (e.g. cells 13, 40, 42, 50, 73, 74), denser than in anaesthetized mice. (e) (i) (Top) Specificity of enhanced responding mitral and tufted cells as a function of the targeted glomerulus ($N = 6$ mice; 27 responsive and specific glomeruli / 46 photo-stimulated target glomeruli; 856 mitral & tufted cells). Note that most cells were non-responsive, or responded specifically to the photo-stimulation of the target glomerulus (13 % of cells had off-target responses to more than one glomerulus; see **Fig. S4a**, Methods); (Bottom) Same for suppressed responses. (ii) (Top) Number of observed sister cells (enhanced responses) per glomerulus photo-stimulation across fields of view (Left; 6.9 ± 6.0 , $N = 27$ FOVs); (Bottom) Number of cells whose baseline fluorescence was suppressed upon photo-stimulation of the same glomeruli (Right; 3.2 ± 2.3 , $N = 20$ FOVs); (iii) (Top) Pairwise distance between sister cells vs. between any cells in the field of view ($142.6 \pm 82.1 \mu\text{m}$ vs. $137.7 \pm 71.8 \mu\text{m}$; 725 vs. 29,850 pairs). (Bottom) Pairwise distance between suppressed cells vs. any cells in the field of view ($116.2 \pm 58.6 \mu\text{m}$ vs. $138.2 \pm 70.4 \mu\text{m}$, 83 vs. 19,607 pairs). Unless specified Avg. \pm SD values are shown. (f) Photo-stimulation of individual (non-parent) glomeruli triggered inhibitory responses in only a small subset of the sister cells of a given identified cohort (Avg. \pm SEM, $14.0 \pm 2.7 \%$, $N=6$).

313 On average, across experiments (10 FOVs, 6 mice, 27/46 response evoking glomeruli) we
314 identified 6.9 ± 6.0 (Avg. \pm SD) *sister* mitral and tufted cells per glomerulus (4 SD response
315 threshold, see Methods). Consistent with previous literature^{36,56,58,75,76}, *sister* cells were spread
316 across the field of view and spatially intermingled with cells receiving inputs from other glomeruli
317 (*non-sisters*) (Avg. \pm SD: 142.6 ± 82.1 μ m pairwise distance between *sister* cells vs. 137.7 ± 71.8
318 μ m between any cells in the FOV). Note that the statistics reported here underestimate the number
319 of *sister* cells per glomerulus⁵⁸ simply because of the limited number of different depths (z-optical
320 planes) and the size of fields of view sampled for this experiment.

321 In addition to light-triggered excitatory responses, we also observed sparse light-induced
322 suppression of the baseline fluorescence in 3.2 ± 2.3 cells per glomerulus. These suppressed cells
323 were intermingled with the identified *sister* cells, and peppered the fields of view (3 SD response-
324 to-baseline signal threshold; 116.2 ± 58.6 μ m pairwise distance of suppressed cells vs. $138.2 \pm$
325 70.4 μ m between any cells in the field). We interpret the observed decrease in M/T resting
326 fluorescence as the suppression of respiration-locked baseline firing patterns⁷⁷⁻⁷⁹ due to lateral
327 inhibition from the photo-stimulated glomeruli acting via local bulbar circuits. Interestingly, we
328 could also observe such light-triggered suppression for a subset of the *sister* cell cohorts (6/27
329 *sister* cell cohorts) identified via *ADePT*. This allowed us to assess whether *sister* cells receive
330 lateral inhibitory inputs from the same or different glomeruli. Photo-stimulation of individual, *non-*
331 *parent* glomeruli inhibited a small fraction of *sisters* within a cohort (1-2 *sisters* per cohort; Avg.
332 \pm SEM, 14.0 ± 2.7 %, N=6, **Fig. 5f**, Methods). In rare instances, where we observed inhibition in
333 2 or more *sister* cells, we found that different *sister* cells were suppressed by photo-stimulation of
334 different individual glomeruli (**Fig. S4f**). These data indicate that indeed *sister* cells, while sharing
335 excitatory drive from the same parent glomerulus, receive sparse inhibitory inputs from different

336 sets of non-parent glomeruli. This is in agreement with previous reports of differences in *sister*
337 cells spike-timing across the respiration cycle^{36,55,70}. While further investigation is needed to
338 understand the logic of these lateral inhibitory interactions, these experiments show that *ADePT* is
339 well-suited for direct mapping of excitatory/inhibitory connections in layered neuronal circuits.

340

341 **Application 2: Assessing the spatial heterogeneity of long-range olfactory bulb inhibition**

342 Next, we used *ADePT* to assess the spatial heterogeneity in the impact of
343 GABAergic/dopaminergic (DAT+ cells, historically known as superficial short axon cells), a class
344 of long-range inhibitory interneurons in the glomerular layer, on the activity of mitral and tufted
345 cells. DAT+ neurons integrate excitatory inputs within individual glomeruli and establish chemical
346 and electrical synapses with other interneurons and mitral/tufted cells within other glomeruli
347 located as far as 1.5 mm away^{43,62}. Given these long-range processes, DAT+ cells are thought to
348 re-distribute focal glomerular odor inputs and convey long-range signals across the glomerular
349 layer. Work from our group and others^{42,43,62–65} suggested that DAT+ neurons enable olfactory
350 circuits to negotiate wide variations in odor concentration by implementing a form of global gain-
351 control (divisive normalization)^{42,43,64,80}. However, it remains unclear whether DAT+ cells
352 broadcast inhibitory inputs uniformly within a local neighborhood or act selectively on particular
353 cells that share specific features such as similarity in odor tuning⁸¹. This is due to previous
354 technical constraints in controlling the activity of DAT+ cells in conjunction with simultaneous
355 imaging of activity in the mitral and tufted cells. We used *ADePT* to photo-stimulate DAT+ cells
356 associated with individual glomeruli while monitoring their impact on either the spontaneous or
357 odor-evoked responses of mitral/tufted cells.

358 We first tested the specificity of targeting DAT+ interneurons across glomerular regions of interest
359 using mice co-expressing both an opsin (ChR2-mCherry⁸²) and a calcium indicator (GCaMP6f⁷²)
360 in the DAT+ cells (**Fig. S5a**). We selected individual adjacent glomeruli for photo-activation,
361 triggering and reading out DAT+ cell activity in the same optical z-plane. Through these
362 experiments, we identified a range of light intensities across which the stimulus-responsive area
363 remained confined to the glomerulus targeted for photo-stimulation (**Figs. S5b-e, Methods**).

364
365 To assess the impact of glomerular DAT+ interneurons on the activity of mitral and tufted cells,
366 we used mice expressing an excitatory opsin in DAT+ cells and the calcium indicator GCaMP6f
367 in mitral/tufted cells (DAT-Cre x Thy1GCaMP6f^{72,83} mice injected retro-orbitally with
368 ChrimsonR-tdtomato AAV-PHP.eB:Syn-FLEX-rc[ChrimsonR-tdtomato]^{84,85}, **Fig.S6a, Methods**).
369 We optogenetically activated DAT+ neurons and monitored the ensuing tufted and mitral cell
370 responses 120-275 μm below the photo-stimulated glomeruli (**Fig. 6**). On average, glomerular
371 DAT+ photo-stimulation targeted to *single* glomeruli resulted in dense, but heterogeneous
372 suppression of the *baseline fluorescence* in mitral cells across the field of view (fraction of mitral
373 cells modulated in example field of view: 0.40 ± 0.19 ; $200 \times 200 \mu\text{m}$, 294 cell-mask pairs, **Figs.**
374 **6a-d, S6b-d**). Stimulation of different DAT+ glomerular masks resulted in ensemble mitral cell
375 responses that were significantly different from each other, but more correlated than the average
376 pairwise responses for controls where cell identities were shuffled (**Fig. 6e**; 0.42 ± 0.23 vs. $0.29 \pm$
377 0.19 , $p < 0.001$, Wilcoxon signed-rank test) or across odors (**Fig. 6e**; 0.42 ± 0.23 vs. 0.25 ± 0.35 ,
378 $p < 0.001$, Wilcoxon signed-rank test). As reference, we also calculated a ‘self’ correlation to assess
379 the variability of photo-stimulation responses to the *same* DAT+ glomerular mask across trials
380 (Methods). Responses of mitral cell ensembles across different DAT+ masks were substantially

381 lower than the ‘self’ control (0.42 ± 0.23 vs. 0.81 ± 0.14 , $p < 0.001$, Wilcoxon signed-rank test,
 382 **Figs. S6b**), demonstrating significant impact of DAT+ neurons on OB outputs.

Figure 6

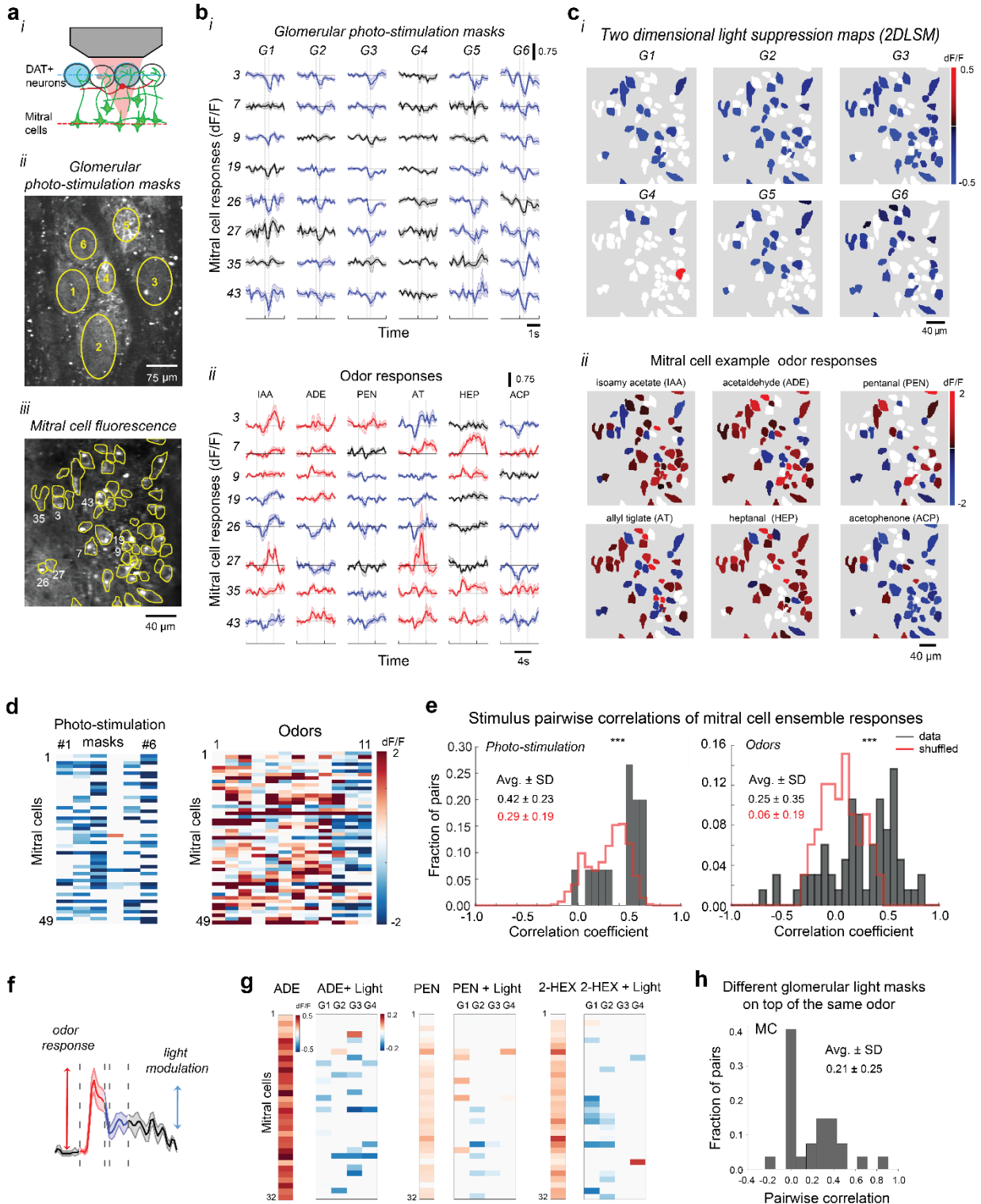


Figure 6. Glomerular photo-activation of DAT+ interneurons triggers dense, but spatial heterogeneous inhibition of mitral and tufted cell activity. (a) (i) Cartoon schematics: photo-stimulation of opsin expressing DAT+ cells while monitoring mitral cell activity (GCaMP6f) by axial decoupling of the photo-stimulation and imaging planes (awake). (ii) Example glomerular field of stimulation; mice express GCaMP6f in mitral and tufted cell glomerular dendritic tufts and ChrimsonR-tdtomato in DAT+ cells (not shown). (iii) Example field of view of mitral cells imaged while photo-stimulating DAT+ cells (200 ms, 7.5 mW/mm²) in the glomerular layer. (b) (i) (Top) Dense, but heterogeneous inhibition of baseline fluorescence in mitral cells across the field of view evoked by photo-stimulation of DAT+ cells across six target glomerular light masks (G1-G6); (Bottom) Odor responses of the same example mitral cells to six odors (isoamyl acetate, IAA; acetaldehyde, ADE; valeraldehyde, PEN; allyl tiglate, AT; heptanal, HEP; acetophenone, ACP). (c) (i) (Top) Fluorescence changes (two dimensional light suppression maps) in mitral cells evoked by photo-stimulation of DAT+ cells across six individual glomerular light masks (G1-G6); (Bottom) Diversity of same mitral cell responses to six example odors (b); each cell in the field of view is displayed on a blue-to-red color scale indicating its response amplitude to light/odor stimulation; non-significant responses were thresholded to white (Methods). (d) Peak fluorescence changes (dF/F) of same mitral cells (49) across the field of view in response to glomerular DAT+ cells photo-stimulation (Left) and to a panel of eleven odors (Right). (e) (Left) Correlation distribution of mitral cell ensemble responses across different pairs of DAT+ cell glomerular photo-stimulation masks (G1-G6). (Right) Same across pairs of odors in the panel (1-11). Shuffled mitral cell index control distributions are shown in red; ‘self’ control (see Fig. S6b-d). (f-h) anaesthetized, also see Fig. S7a-f; (f) Fluorescence change (dF/F) elicited by odor presentation in one example tufted cell, and its subsequent modulation by projecting a glomerular light mask to optogenetically augment DAT+ cell activity (500 ms, 10mW/mm²; 2s from odor onset). (g) Mitral cell peak odor responses (ADE, PEN, 2-HEX) and their modulation by 4 glomerular DAT+ cell glomerular light masks in an example field of view (Fig. S7). (h) Stimulus response pairwise correlations of mitral cell ensembles: distribution of pairwise correlations for different glomerular DAT+ cells photo-stimulation masks imposed on top of the same odor aggregated across the three odors in (g) (0.21 ± 0.25 ; 27 pairs, 2 FOVs, 39 MC cells).

383 Stimulation of DAT+ neurons results predominantly in the suppression of mitral and tufted cells
384 from their baseline activity. To boost the baseline M/T cell fluorescence and better characterize
385 the impact of DAT+ neurons, we presented odors (4s) in conjunction with DAT+ cell photo-
386 activation in the middle of the odor presentation period. Similar to the experiments described above
387 (Figs. 6a-e), stimulating DAT+ cells across different glomeruli during odor presentation also
388 resulted overall in differential suppression of the OB outputs (Figs. 6f-h, S7a-f, TC: 0.44 ± 0.33 ;
389 MC: 0.21 ± 0.25 ; pairwise correlation, $p < 0.001$, Wilcoxon signed-rank test; modulation by light on
390 top of odor: 78.0 % unmodulated, 18.2% suppressed vs. 3.8% enhanced MC-odor-pairs; N=2,214

391 pairs; and 54% unmodulated, 42.6% suppressed vs. 3.4% enhanced TC-odor pairs, N = 945 pairs).
392 Thus, we find that the impact of DAT+ cells on the OB output is dense, but locally heterogeneous
393 with different cells exhibiting diverse sensitivities to DAT+ inhibition originating from a given
394 glomerulus (**Fig. 6**). Further investigation will determine whether DAT+ cell action shapes the
395 MC and TC cell odor responses in a systematic manner as a function of similarity in their odor
396 responses.

397
398 In summary, we show that *ADePT* can be flexibly combined with genetic strategies and/or sensory
399 stimuli to probe the contribution of both excitatory and inhibitory neuronal types in shaping the
400 output of optically accessible neuronal circuits.

401

402 **Discussion**

403 We demonstrate a readily implementable method (*ADePT*) for optical control and recording of
404 activity in three-dimensional neural structures by decoupling the focal planes for optogenetic
405 patterned stimulation and multiphoton imaging. When referenced to other comparable
406 techniques^{8,9,13,20–22,29–33}, *ADePT* enables us to control neuronal activity across a wide field of view,
407 does not suffer from aberrated imaging, and is easy to implement. We confirmed that we were able
408 to maintain precise spatial control over a range of activation powers and demonstrated the
409 usefulness of the system by mapping *both excitatory and inhibitory* functional connectivity in the
410 mammalian olfactory bulb.

411

412 *ADePT* allows arbitrary axial shifting of 2D photo-stimulation light patterns of choice relative to
413 the focal plane of the imaging objective by translating a motorized diffuser along the photo-

414 stimulation optical path (**Fig. 1**). As a function of its angular divergence, the choice of the diffuser
415 determines the degree of axial confinement of the photo-stimulation pattern, enabling optical
416 sectioning in the widefield illumination configuration, and also increasing homogeneity in the
417 photo-stimulation patterns (**Figs. 2,3**). The larger the angular divergence of the diffuser, the tighter
418 the axial extent of the pattern, which comes at the expense of excitation light loss. In our
419 implementation, we controlled glomerular activity optogenetically over a 1.5 x 1.2 mm field of
420 stimulation with ~ 20 μm lateral and ~ 40 μm axial resolution. Different magnification choices in
421 the photo-stimulation path, however, can be used to customize the extent of the field of stimulation
422 with inherent resolution trade-offs. In its current implementation, *ADePT* does not afford the
423 resolution to optogenetically target individual cells, but is effective in controlling the activity of
424 larger input units (e.g. single olfactory glomeruli, whisker barrels) in neural circuits of interest,
425 while monitoring their impact across different cell types at cellular resolution via multiphoton
426 imaging of changes in activity. Furthermore, different choices of the diffuser enable tighter axial
427 resolution at the expense of photo-stimulation light loss (grit ground diffuser vs. holographic
428 diffusers, **Fig. 2**). While achieving axial-confinement of extended 2D photo-stimulation patterns
429 (**Fig. 2**), *ADePT* is effective for optical control of activity largely in the superficial brain layers,
430 since it is constrained by light scattering-related degradation (**Fig. S2**).

431

432 In proof-of-principle experiments, we used *ADePT* to investigate the functional connectivity of
433 olfactory bulb circuits in the mouse. We controlled optogenetically the activity of select excitatory
434 and inhibitory cell types in the input layer (OSNs vs. GABAergic/dopaminergic DAT+
435 interneurons) at *sub-glomerular* resolution, while monitoring their impact on the responses of the
436 principal neurons (mitral and tufted cells). By targeting optically addressable glomeruli (**Figs. 4,5**),

437 we identified multiple cohorts of daughter *sister* mitral and tufted cells driven by *parent* glomeruli
438 and revealed sparseness and differential action in the olfactory bulb inhibitory lateral interactions
439 (**Fig. 5**). Our approach further enables discriminating between different inhibitory inter-glomerular
440 connectivity schemas (e.g. uniform vs. heterogeneous) implemented by different cell populations
441 (e.g. GABAergic/dopaminergic DAT+ interneurons), and testing hypotheses on how connectivity
442 relates to the similarity in odor response tuning. We found that DAT+ cells associated with
443 different glomeruli mediate dense, but heterogeneous (non-uniform) suppression of MC and TC
444 baseline and odor responses (**Fig. 6**).

445
446 Compared to previous work on mapping individual glomerular outputs^{36,55}, *ADePT* affords one-
447 to-two orders of magnitude higher throughput and cell type specificity in the activity readout.
448 Identifying multiple cohorts of *sister* cells is key for determining the specificity of inhibitory inputs
449 that principal OB neurons integrate to compute relevant stimulus features. As previously
450 proposed^{36,56}, we found that *sister* cells, driven by the same *parent* glomerulus, receive differential
451 inhibitory input from other glomeruli with implications for odor coding. As such, many more
452 output information channels may leave the bulb than then number of input sensory afferent types.
453 Increasing the number of *sister cell cohorts* mapped to their *parent* glomeruli, and systematic
454 photo-stimulating spatial-temporal combinations of multiple (*non-parent*) glomeruli will enable
455 further testing hypotheses on how inhibitory connectivity relates, for example, to the degree of
456 similarity in the odor responses of the corresponding input glomeruli. In recent sequencing-based
457 single-cell projection mapping, we identified structure in the projections of individual mitral cells
458 at different locations along the A-P axis of the piriform cortex with respect to their co-projections
459 to extra-piriform target regions^{86,87}. By combining functional mapping and anatomical DNA

460 barcoding projection mapping approaches, future work will determine whether the *sister* outputs
461 of individual glomeruli segregate into parallel functional streams that may support different
462 computations related to perception versus valence versus action⁸⁷ during odor-guided behaviors.

463
464 More broadly, simultaneous patterned photo-stimulation and multiphoton imaging in different
465 axial planes enables mapping functional connectivity not only in the olfactory bulb, but can be
466 implemented between any optically accessible brain regions (across layers) including the
467 neocortex. For example, *ADePT* is well positioned for mapping functional connectivity in the
468 barrel cortex within and across barrels^{34,88}, as well as bidirectional interactions between cortical
469 visual areas (V1 vs. PM, AL, etc.)^{89,90}, visuomotor (M2-V1)⁹¹⁻⁹³ or audiomotor circuits (M2-
470 A1)^{94,95}, etc. Given its relative simplicity, cost-effectiveness, and ease-of-use, compared to other
471 axially decoupling optical imaging and photo-stimulation strategies, *ADePT* is readily applicable
472 for investigating the logic of neural connectivity.

473

474

475 **Acknowledgements:** The authors acknowledge R. Eifert and D. Cowan for technical support. This
476 work was supported by NSF IOS-1656830 to D.F.A. and Beckman Institute CLOVER
477 (CLARITY, Optogenetics, and Vector Engineering Research) to V.G.

478

479 **Data and code availability:** All data matrices included in the analyses presented here representing
480 mitral/tufted and GABAergic/dopaminergic DAT+ interneuron GCaMP responses triggered by
481 odor and optogenetic light stimuli, as well as the code used for the instrument control and analysis
482 are available upon request.

483 **Declaration of interests:** The authors declare no competing interests.

484

485 **Authors contributions:** conceptualization, investigation, methodology, formal analysis,
486 visualization, software, data curation and writing, M.K., F.A.; methodology, formal analyses,
487 visualization, data curation, validation, software, S.K.K., S.S.T; methodology, visualization,
488 validation, D.E.H., W.G.B., P.S.V., H.C, M.B.D.; reagents development, Z.Q., V.G.;
489 conceptualization, methodology, formal analysis, visualization, and writing, A.B.;
490 conceptualization, methodology, formal analysis, visualization, software and writing, P.G.;
491 conceptualization, methodology, investigation, methodology, writing, supervision, project
492 administration, and funding acquisition, D.F.A.

493

494

495 **Methods**

496 **Combined two-photon imaging and photo-stimulation microscope:** For *two photon imaging*
497 (**Fig. 1b**), the output from a Ti:Sapphire laser (Coherent Chameleon Ultra II) was magnified by a
498 1.5x beam expander (L1, L2, focal lengths, FL: 40, 60 mm), then reflected off two mirrors
499 (10D20ER.4, Newport) and a periscope onto a galvanometric mirror scanning system (GM,
500 6215HB, Cambridge Technologies). The semi-stable stationary point between the GM was
501 expanded and imaged to fill the back aperture of the microscope objective by a telescope (L3,
502 AC300-050-B, L4, AC508-300-B, FL 50, 300 mm, Thorlabs). The objective and microscope stage
503 were mounted on motorized linear translators (x-y stage: 462-XY-M; z-stage: CMA-25CCCL,
504 Newport) connected to a three-axis motion controller (Newport ESP301). Fluorescence light from
505 the sample was collected by the objective, then reflected by a dichroic mirror (DM1, 680dcxr, 50

506 mm diameter, Chroma) placed atop of the imaging objective (Olympus 20x 1.00 NA
507 XLUMPlanFLN) and a second short-pass dichroic mirror (DM2, 505 nm, FF505-SDi01-50.8-D,
508 50 mm diameter, Semrock) towards a GaAsP PMT (H11526-20-NF, Hamamatsu) for green or
509 red fluorescent detection (sliding holder, LCFH2 green, FF03-525/50-25 and red, FF01-607/70-
510 25 emission filters, Semrock). The back aperture of the microscope objective was imaged into the
511 PMT aperture by a telescope (L5/L6, FL: 100/32 mm; L5 – LA4545-A (UV fused silica); L6 -
512 AL4532-A, Thorlabs). The current output of the PMT was transformed to voltage, amplified
513 (SR570, Stanford Instruments) and digitized using a data acquisition board (NI-PCI-6115,
514 National Instruments). The same board was also used to generate signals for controlling the
515 galvano-metric mirrors. By rotating DM2 by 90° on a custom holder (CSHL, Machine Shop), light
516 was directed either to the PMT or to a CCD camera (Vosskuhler 1300-QF, **Fig. 1**). The image of
517 the sample was further minified by a telescope (L7/L8, focal lengths: 100/40 mm) and captured on
518 the CCD chip (CCD 1), allowing for a larger field of view of approximately 1,500 x 1,200 μm.
519 Additional short pass filters (FF01-750/SP-50, 50 mm diameter, Semrock) were used in front of
520 light detectors (CCD and PMTs) to block stray light from the infrared multiphoton excitation laser.
521 For *patterned photo-stimulation*, the beam from a 488-nm laser (Coherent Sapphire 488, 200mW)
522 was magnified using a beam expander (L12/L11, FL: 30/300 mm) and reflected by a mirror and a
523 periscope (RS99, Thorlabs) onto the surface of a DMD chip (DMD 0.7” XGA VIS, Vialux GmbH,
524 1024 x 768 pixels, 13.68 μm micro-mirror pitch). The DMD chip was controlled using a Vialux
525 DLP-Discovery 4100 board and the corresponding application programming interface (Vialux
526 GmbH). To obtain direct access to the chip, we removed the projecting lens and prism installed in
527 front of the DMD by the manufacturer. The steep angle of incidence of the photo-stimulation beam
528 onto the DMD was carefully tuned to ensure maximal diffraction efficiency. The patterned beam

529 reflected off the DMD was further magnified by a L10/L9 telescope (FL 100/200 mm), and
530 coupled into the microscope by DM1. An iris (SM2D25, Thorlabs) was placed at the front focal
531 plane of L10 to block the higher diffraction order replicas of the DMD-generated spatial pattern.
532 The photo-stimulation pattern was further projected into the sample by the tube lens (L5, FL 100
533 mm) and the principal objective (Olympus 20x 1.00 NA XLUMPlanFLN).

534

535 **Diffuser:** A diffuser was used to axially confine the photo-stimulation pattern. The diffuser was
536 mounted on a translational stage (Newport, 433-series, #BZA647202) connected to a stepper
537 motor. The motor was controlled using an open source Arduino-based system⁹⁶. In the home
538 position (imaging and photo-stimulation planes superimposed), the diffuser sits at the focal plane
539 of the tube lens L5. Three different round diffusers (25 mm diameter) were tested, as detailed in
540 the text: two holographic diffusers with 5° and 10° divergence angle (5° - #55-849, 10° - #48-506,
541 Edmund Optics), and a grit ground glass diffuser (#38-786, Edmund Optics). Two fast shutters
542 (Uniblitz VS14) were placed in front of the PMT and the blue photo-stimulation laser respectively,
543 and operated in anti-phase so that only one shutter was open at a time such as to alternate between
544 periods of photo-stimulation and photon collection.

545

546 **Excitation power control and lenses:** The excitation two photon laser power was controlled by a
547 Pockels cell (Conoptics 350-80 BK) placed in the imaging path. An additional filter (775 nm long
548 pass, 25 mm diameter, #86-069, Edmund Optics) was added to the excitation path to block a
549 residual red component from the Ti:Sapphire laser, that would otherwise saturate the red PMT.
550 When required, additional neutral density filters (Thorlabs, NDK01) ranging from ND 0.2 to ND
551 2.0 were added to the photo-stimulation path to further reduce the power. All lenses (Thorlabs)

552 had anti-reflective coating for either infrared (imaging path) or visible (photo-stimulation and
553 detection paths) light. A UV fused silica lens was used instead of the more common N-BK7 lenses
554 in position L5 (LA4545-A) to avoid spurious phosphorescence signals following illumination with
555 intense blue light pulses (see *Phosphorescence Artifacts*).

556

557 **Auxiliary microscope:** An auxiliary microscope was used during characterization experiments,
558 as described in *Lutz, et al. (2008)*⁶. We placed a secondary objective, tube lens and green emission
559 filter (HQ510DCLP, Chroma) below the main imaging objective to image the focal plane of the
560 main objective onto a CCD camera (Vosskuhler 1300-QF, **Fig. 3a**). Depending on the experiment,
561 different objectives (Olympus 4X, 0.13 NA UPlanFIN or Olympus 20X, 0.50 NA UPlanFIN) were
562 used in combination with a 150 mm focal length tube lens to obtain either a minified image of the
563 entire field of photo-stimulation or a higher resolution image of a smaller field. The microscope
564 framework was constructed with a Thorlabs 2" cage system. The secondary objective was held
565 either by a kinematic mount for fine tilt adjustment (KC2-T, Thorlabs), or by a laterally-
566 translatable platform. The photo-stimulation patterns were imaged onto a coverslip spin-coated
567 with a thin (~1 μm) rhodamine B layer (courtesy of V. Emiliani, Paris Descartes University).

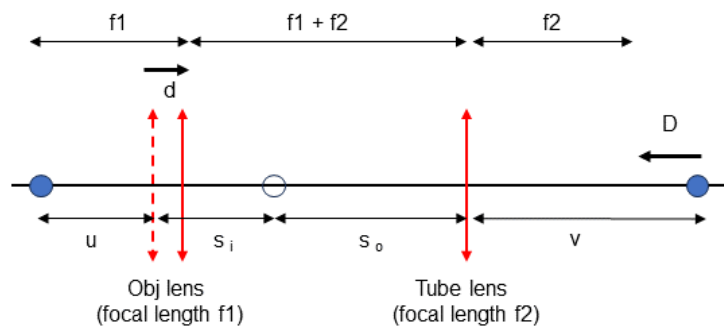
568

569 **Calibrating decoupling of photo-stimulation and imaging planes:** We used the auxiliary
570 microscope to calibrate the decoupling of photo-stimulation and imaging planes (**Fig. 3a**). Initially,
571 the diffuser was positioned at a plane conjugated to the focal plane of the principal and auxiliary
572 objectives, and the photo-stimulation pattern was in focus on the coverslip, appearing sharp both
573 on the principal (primary) and the auxiliary (secondary) CCD cameras (**Fig. 3a, Left**). The principal
574 objective was then moved closer to the coverslip to simulate shifting the imaging plane to deeper

575 layers in a biological preparation. At this point, the photo-stimulation pattern was still imaged
576 (projected into sharp focus) on the focal plane of the principal microscope objective (now below
577 the coverslip), and no longer in focus on the secondary CCD camera. To move the photo-
578 stimulation pattern back to the initial position, we moved the diffuser away from the tube lens (L5)
579 until the projected pattern was again in focus on the fluorescent coverslip and on the secondary
580 CCD camera (**Fig. 3a, Right**). Using this strategy, we iteratively constructed an empirical
581 calibration curve that relates the diffuser displacement to the position of the photo-stimulation
582 plane in the sample with respect to the focal/image plane of the principal objective (**Fig. 3b**).

583

584 **Relating movement of the objective to the adjusting displacement of the diffuser:** Within the
585 thin lens approximation framework, let u be the distance between the objective (O) and the image
586 of the projected light pattern, $s_i + s_o$ the distance between the objective and the tube lens (L5), v the
587 distance from the diffuser to the tube lens, and f_1 and f_2 the focal lengths of the objective and the
588 tube lens.



589 How does the displacement of the objective (d) relate to the displacement of the diffuser (D)
590 needed to bring the projected pattern in focus in the desired z -plane in the sample, as a function of
591 magnification (M) of the system given by the ratio of focal lengths of the tube lens and objective
592 lens ($M=f_2/f_1$)?

593
$$v = \frac{u * f}{u - f} \quad \text{Eq. 1}$$

594 Calculating image distance ($u = f1 - d$) for the objective lens (O), when d is small:

595
$$s_i = \frac{(f1 - d) * f1}{(f1 - d - f1)}$$

596
$$s_i = -\frac{(f1 - d) * f1}{d} \quad \text{Eq. 2}$$

597 For the tube lens, the object distance is: $s_o = (f1 + f2 + d) - s_i$

598

599 Replacing s_i from Eq. 2:
$$s_o = (f1 + f2 + d) + \frac{(f1 - d) * f1}{d}$$

600

601 Since d is small, ignoring higher order terms of d , we obtain:

602
$$s_o = \frac{f1^2 + f2 * d}{d} \quad \text{Eq. 3}$$

603 For the tube lens, image distance (v) is given by:

604
$$v = f2 + D = \frac{s_o * f2}{s_o - f2}$$

605

606 Solving for D :
$$D = \frac{s_o * f2}{s_o - f2} - f2$$

607
$$D = \frac{f2^2}{s_o - f2} \quad \text{Eq. 4}$$

608 Replacing s_o and solving for D :

609
$$D = \left(\frac{f2}{f1}\right)^2 * d \quad \text{Eq. 5}$$

610 Therefore, we find that the axial displacement of the photo-stimulation plane at the sample (d) is

611 linearly proportional to the translation of the diffuser in the optical path (D).

612

613 **Photo-stimulation and imaging calibrations**

614 ***DMD-chip to CCD-chip to multiphoton image registration:*** To photo-stimulate specific locations
615 in the sample, we determined where a given *pixel on the DMD* falls on the *specimen* using the
616 primary camera (CCD1) as a reference. After registering pixels on the DMD-chip to CCD1 chip
617 pixels, a point-to-point correspondence between the DMD-chip and the focal plane of the principal
618 objective was obtained. Further, the auxiliary microscope was used to map the correspondence
619 between pixels on the *DMD* and the *specimen* in z-planes out of the focal plane of the principal
620 objective. To map pixels in the *two photon field of view* to the *DMD*, we also used CCD1 as
621 intermediary reference. Within this frame of reference, we targeted ROIs that were axially (z)
622 displaced from the principal objective focal plane, and imaged either using the primary CCD
623 camera or the two photon microscope. Pixels of the DMD-chip were mapped onto pixels of CCD1
624 by projecting a series of light spots generated from known DMD locations. Routinely, we placed
625 20 μm sized spots in a 4 x 5 grid spanning the field of stimulation. After recording the position of
626 all these fiduciary light spots, we computed the 3 x 3 matrix $\mathbf{T} = \mathbf{D}\mathbf{C}^T(\mathbf{C}\mathbf{C}^T)^{-1}$, where \mathbf{C} and \mathbf{D} are
627 $N \times 2$ matrices whose rows contain the light spot coordinates on the CCD1 and DMD chips
628 respectively. The matrix \mathbf{T} , when left-multiplied with CCD1 chip coordinates, transforms CCD1
629 coordinates into DMD-chip coordinates. To verify this procedure, a high-density sample with 15
630 μm fluorescent latex microbeads was imaged using first the widefield fluorescence path (CCD1),
631 and subsequently the two photon microscope. Individual microbeads were matched between the
632 acquired images manually (*cpselect* tool in the MATLAB image processing toolbox). We obtained
633 a look-up table of two photon / CCD1 images point pairs. Further, by minimizing the sum of
634 squared errors, we calculated the corresponding transform matrix that maps two photon image
635 pixels onto CCD1 image pixels. The absolute position of a particular location in a two photon

636 image is dependent on both the field of view and the resolution settings (number of pixels) of the
637 image. Several FOV and pixel resolution settings were chosen for registration, and further used
638 accordingly when targeting ROIs within a two photon reference image. Post-registration, we
639 verified that the targeting of the DMD-chip generated patterns was precise. The control software
640 reproduced the desired target light spots with high accuracy within the field of stimulation, using
641 only the two photon image or only the CCD1 image as guide; error between projected centroids
642 light spots vs. fluorescence microbeads was less than 5 μm , **Figs. 1d, S1d**.

643

644 **Correcting the field of photo-stimulation power inhomogeneity:** Due to the Gaussian intensity
645 profile of the blue laser beam illuminating the DMD chip, the power towards the borders of the
646 field of photo-stimulation is lower than in the center. To correct for this inhomogeneity, and ensure
647 flatness of photo-stimulation across the field, we calculated a power distribution map (PDM)
648 across the field of stimulation, obtained by sequentially projecting 25 μm spots in an 11 x 11 grid
649 pattern covering 121 pixel coordinates across the DMD-chip, and by linearly interpolating such as
650 to estimate the power at the remaining positions. We projected the spot pattern on the DMD chip
651 and placed a power sensor (Thorlabs, 50mW, S120B) under the primary objective with the pattern
652 in focus. For simple patterns, such as spatially-localized single spots, the laser power can be
653 adjusted accordingly using the PDM look-up table to compensate for power loss at the borders.
654 For more complex light patterns, where different regions of the pattern have different local light
655 intensities, pulse-width modulation can be used to control the average light intensity experienced
656 by each spot independently.

657

658 **Off-focal plane aberration correction:** We often presented a spatial photo-stimulation pattern
659 based on glomerular shapes on the brain surface, while imaging deeper structures, such as mitral
660 and tufted cells, which resulted in small, but significant changes in the size of the projected pattern
661 (i.e. DMD-generated optogenetic stimulation pattern is in focus above the focal plane of the
662 principal imaging objective). We compensated for this change in magnification by another linear
663 transformation that we measured using the auxiliary microscope mounted beneath the principal
664 microscope. The same procedure described above for mapping DMD-chip pixels to the primary
665 camera (CCD1) was repeated using the secondary camera (CCD2) at several focal plane
666 displacements in steps of 100 μm (e.g. 0, 100, 200...500 μm) and a corresponding set of
667 transformations $T(0), \dots, T(N)$ from the DMD-chip pixels to the secondary camera (CCD2) pixels
668 was obtained. For each such transformation, we isolated the effect of changing displacement by
669 multiplying the inverse of the zero-axial displacement transformation to obtain a set of “depth
670 transformations” $B(0), \dots, B(N)$. The depth transformation for arbitrary depths was calculated by
671 linearly interpolating between the measured transformations.

672

673 **Dichroic mirror offset:** When registering the primary camera (CCD1), the dichroic mirror (DM2)
674 must be positioned to direct light from the sample onto the primary camera. However, light from
675 the DMD-chip is refracted as it passes through the dichroic mirror, causing the photo-stimulation
676 pattern to be translated when DM2 is rotated by 90 degrees towards the PMT. We measured the
677 displacement by projecting a square light pattern and recording an image with the auxiliary
678 microscope with the dichroic positioned towards the CCD1 or the PMT. Identifying a corner of
679 the projected square light pattern across the two images allowed using the secondary camera
680 CCD2-to-DMD-chip registration to determine the dichroic induced offset in projection.

681

682 **Lateral spot size measurement:** To calculate the full-width at half maximum (FWHM) in the
683 lateral direction (**Figs. 2a-c**), we projected a circular spot onto a rhodamine B-coated coverslip and
684 acquired images with the auxiliary microscope. We thresholded each image and found the center
685 of the spot by computing a weighted centroid of the thresholded image:

686

$$c = \operatorname{argmax}_x \sum_x I(x)x$$

687 where x is a vector containing the pixel coordinates and $I(x)$ is the brightness of the image at point
688 x . The threshold was chosen heuristically by visual inspection of a single image and finding a value
689 which isolated the light spot, and which, when changed by small amounts, did not significantly
690 change the position of the centroid. We generated and averaged a set of line profiles passing
691 through the centroid rotated in 1° increments over 360° . The resulting symmetric line profile was
692 further used to compute the FWHM.

693

694 **Axial spot size measurement:** To measure the axial (z) profile of the projected light spots, we
695 brought different axial sections of the spots into the focal plane of CCD2 by stepping the principal
696 objective up and down over an interval of $\pm 100 \mu\text{m}$ (for spots of diameter $\leq 40 \mu\text{m}$) or over ± 200
697 μm range (for spots of diameter $> 40 \mu\text{m}$) in z increments of 1 and 2 μm respectively. We defined
698 a region of interest (ROI) for analysis by taking all points within the FWHM of the spot in the
699 central section. The axial profile was defined as the intensity within the ROI across all sections
700 (**Figs. 2a-c**). To estimate the effect of spherical and other types of aberrations, we measured the
701 axial profile of our projected spots for photo-stimulation plane z offsets of $\Delta z = 0 - 400 \mu\text{m}$ with
702 respect to the focal plane of the principal objective (**Fig. 3c**). For these measurements, we used
703 spot diameters of 30, 60 and 90 μm respectively. Since in these configurations the diffuser is not

704 positioned at a plane conjugate to the focal plane of the principal objective, any relative movement
705 of the principal objective with respect to the tube lens L5 results in a slight change in magnification.
706 The projected light spot size was corrected accordingly for the predicted increase in magnification.

707

708 **Optical alignment.** Alignment of the two-photon microscope followed the typical procedure⁹⁷.

709 The photo-stimulation beam was further aligned on the DMD chip. In our implementation, the
710 DMD chip was mounted onto an articulating base-ball stage (SL20, Thorlabs) that can be raised
711 and lowered. We used a periscope (RS99, Thorlabs) formed by two mirrors placed on kinematic
712 mounts to center the photo-stimulation laser beam on the DMD chip. By applying an all-white
713 pattern to the DMD-chip, a coarse alignment was obtained with the light reflected off the DMD-
714 chip into the microscope and the photo-stimulation beam centered on the chip. One point of
715 potential difficulty in the alignment procedure is given by the diffractive behavior of the DMD-
716 chip when illuminated with coherent light. The face of each individual micro-mirror is offset with
717 respect to the plane of the entire array of mirrors. Because of this, the DMD-chip behaves like a
718 blazed diffraction grating. We aligned the blue laser beam such that most of the power is sent into
719 a particular diffraction order. For a one-dimensional grating, the angle θ_m of diffraction order m is
720 given by:

721
$$m\lambda = d(\sin \theta_i + \sin \theta_m)$$

722 while θ_r , the angle at which the reflected laser power leaves the DMD chip is given by:

723
$$\theta_r = 2\alpha - \theta_i$$

724 where θ_i is the incident angle with respect to the normal of the grating, λ is the wavelength, d is the
725 grating spacing, and α is the offset or “blaze angle” of the mirror face relative to the grating. Since
726 the micro-mirrors rotate along one diagonal of the mirror, the projection of the correct incident

727 angle onto the mirror face must lie orthogonal to this diagonal. This line was determined by
728 toggling all the mirrors between the on and off positions (setting an all-white or all-black image)
729 and observing where the light is redirected.

730 To make final adjustments to the position, we compared the power in the brightest diffraction order
731 to the four adjacent ones. We then adjusted the incident angle of the beam by tilting or translating
732 the DMD-chip mount and compensating with the periscope mirrors to keep the photo-stimulation
733 beam centered until the power in the brightest spot was maximally bright relatively to its neighbors.
734 After optimizing the incident angle, the brightest spot was ~ 60% as powerful as before the DMD
735 chip. A circular iris (SM2D25, Thorlabs) was used to block out light from other diffraction orders.
736 Applying a cross-shaped or small circular pattern to the DMD chip is useful for determining the
737 center of the field of stimulation. Finally, the dichroic mirror (DM1, **Fig. 1**) was used to align the
738 center of the photo-stimulation pattern to the same vertical line as the two-photon beam, and the
739 primary camera (CCD1) and PMTs were placed and aligned as described above.

740

741 **Propagation of patterns through brain tissue:** We used the auxiliary microscope to characterize
742 how the lateral profile of the one photon extended (2D) photo-stimulation patterns deteriorates
743 after propagation through brain slices of different thicknesses, following the procedure described
744 in *Papagiakoumou et al., 2013*⁶⁹. Adult mouse brains were fixed with paraformaldehyde and slices
745 cut to various thicknesses. After focusing the photo-stimulation pattern on the fluorescent coverslip
746 so that it was in focus on both the primary and the secondary cameras, we placed a slice on the top
747 of the coverslip with the pattern illuminating the olfactory bulb. The photo-stimulation light
748 travelled through the slice and was scattered by the tissue before the pattern was imaged on the
749 coverslip and the secondary camera (CCD2). We took a total of six measurements for each slice

750 thickness (three positions, two slices). We used as reference for normalization the configuration
751 when no slice was present (0 thickness) and defined the ROI for analysis as the set of points within
752 the FWHM when no slice was present. We then calculated the light intensity and the standard
753 deviation of pixel values within the ROI and compared it to values obtained for different slice
754 thicknesses (**Figs. S2c-g**).

755

756 **Phosphorescence artifacts.** We observed a small slowly-decaying PMT signal upon illumination
757 with the blue photo-stimulation laser in the absence of a fluorescence specimen. By progressively
758 blocking off different parts of the optical path, we determined that the main contributors to this
759 signal were the objective and tube lens (O and L5 in **Fig. 1**). Upon replacing the N-BK7 glass tube
760 lens (LA1384-A) with a fused silica lens (LA4545-A) with the same focal length, the signal
761 dropped substantially (**Fig. S1e**). The artifact was not affected by the type of anti-reflective coating
762 used (**Fig. S1e**). We tested several objectives (Olympus 20x 1.00 NA XLUMPlanFLN, Olympus
763 20x 0.95 XLUMPlanFL, Olympus 25x 1.05NA XLPlanN) and determined that they contributed
764 differentially to this signal. Of these, the 25x fared best followed by the 1.0 NA 20x and the 0.95
765 NA 20x (data not shown). Following this optimization, when comparing identified cells to
766 background areas in our imaging experiments, we could not detect any spurious signals in
767 background selected areas.

768

769 **Mice:** For the *in vivo* experiments described here, we included data from 12 OMP-Cre x ReChr x
770 Thy1GCaMP6s mice, 3 DAT-Cre mice and 4 DAT-Cre x Thy1-GCaMP6f mice. For experiments
771 to map mitral/tufted cell parent glomeruli and identify *sister* cell cohorts, triple mouse crosses
772 (OMP-Cre x Rosa26 CAG-LSL-ReaChR-mCitrine⁷¹ x Thy1GCaMP6s_{4.3}⁷³) were used to

773 express ReaChR-mCitrine and GCaMP6f/s in the OSNs and respectively mitral and tufted cells
774 (**Figs. 4,5**). For experiments expressing ChR2 and GCaMP6f in DAT+ cells (**Fig. S5a-e**), we used
775 mice expressing Cre recombinase in DAT+ neurons and approximately 300 nl of a mixture of
776 AAV (serotype 2.9, UNC Vector Core) virus carrying DIO-ChR2-mCherry and DIO-GCaMP6f
777 was injected into the olfactory bulb at a depth of 300 μm as previously described⁴³. For glomerular
778 stimulation, for each light stimulus other than control stimuli, we fit a function of the form $f(d) =$
779 $Ae^{-d/b}$ where f represents the light-evoked fluorescence change in a region of interest and d is the
780 distance from that region to the center of the projected light mask. The width constant b of this
781 exponential fit gives a measure of the spread of activity evoked by that stimulus. For each light
782 intensity sampled, we repeated the analysis in two different fields of view, and the relationship
783 between activation width and light intensity is shown in **Figs. S5b-e**. As in the case of OSN
784 terminals photo-stimulation experiments, we flashed single 100 ms sub-glomerular light masks
785 (20 μm diameter) between the imaging frames and recorded calcium transients in the DAT+ cells
786 via multiphoton imaging. For analysis, the field of view was divided into a 20 by 20 grid (15 x 15
787 μm grid units), and the response was defined as the average change in fluorescence in each unit of
788 the grid during the two frames (10 Hz) immediately following the light stimulus. We tested a range
789 of photo-stimulation light intensities ranging from 0.5 to 10.0 mW/mm^2 . We tuned up the intensity
790 of the fluorescence response, while aiming to maintain spatial specificity, as indicated by the
791 photo-activated area remaining largely confined to the chosen glomerulus. We quantified the
792 spread of activity by characterizing the relationship between the DAT+ cell response strength and
793 the distance from the centroid of the light stimulus, which was well-fit by exponential decay.
794 Within the range of light intensity used, the characteristic width constant varied from 25 μm for
795 the lowest to 62 μm for the highest.

796

797 For experiments investigating the impact on mitral/tufted cell activity of glomerular
798 GABAergic/DAT⁺-neurons (superficial short axon cells), DAT-Cre mice were crossed to
799 Thy1GCaMP6f_{5.11}⁷³ mice (**Figs. 6, S6, S7**). DAT-Cre x Thy1-GCaMP6f mice were retro-
800 orbitally injected⁹⁸ with 5×10^{12} vp of AAV-PHP.eB:Syn-FLEX-rc[ChrimsonR-tdtomato], which
801 was prepared as previously described^{84,99}. Viral particles were diluted in saline to achieve a final
802 volume of 100 μ L per injected mouse. All animal procedures conformed to NIH guidelines and
803 were approved by the Animal Care and Use Committee of Cold Spring Harbor Laboratory.

804

805 **Surgical procedures:** Mice were injected with NSAID Meloxicam 0.5 mg/Kg (Metacam®,
806 Boehringer Ingelheim. Ingelheim, Germany) 24 hours prior the surgical procedure, at the onset of
807 surgery, and for 2 days *post* each surgical procedure. Depending on the recovery progression, the
808 NSAID treatment was maintained until mice showed alert, and responsive behavior. Before each
809 stereotaxic surgery, mice were anesthetized with 10% v/v Isoflurane (Cat# 029405. Covetrus.
810 Portland, ME, US). For the chronic window and headbar implantation procedures, mice were
811 anesthetized with a ketamine/xylazine (125 mg/Kg - 12.5 mg/Kg) cocktail. During surgery, the
812 animal's eyes were protected with an ophthalmic ointment (Puralube®, Dechra. Nortwich,
813 England, UK). Temperature was maintained at 37 °C using a heating pad (FST TR-200, Fine
814 Science Tools. Foster City, CA, USA). Respiratory rate and lack of pain reflexes were monitored
815 throughout the procedure. Chronic window implant surgeries were supplemented with
816 dexamethasone (4 mg/Kg) to prevent swelling, enrofloxacin (5 mg/Kg) to prevent bacterial
817 infection, and carprofen (5 mg/Kg) to reduce inflammation.

818

819 **Chronic implantations:** After recovery from the stereotaxic surgery, mice were implanted with a
820 custom titanium head bar attached with C&B Metabond Quick adhesive luting cement (Cat# S380.
821 Parkell. Edgewood, NY, USA), followed by black Ortho-JetTM dental acrylic application (Cat#
822 1520BLK. Lang. Chicago, IL, USA) and with a cranial window on top of the olfactory bulb as
823 previously described^{100,101}. Special care was taken to remove the bone under the inter-frontal
824 suture and remove small bone pieces at the edges. During surgery, the exposed olfactory bulb was
825 continuously protected and cleaned of blood excess using artificial cerebrospinal fluid (aCSF) and
826 aCSF-soaked gelfoam. Once both hemibulbs were exposed and clean, a fresh drop of aCSF was
827 placed on top, followed by a 3 mm round cover glass, which was gently pushed onto the OB
828 surface to minimize motion artifacts in further experiments. Once in place, the coverslip was sealed
829 along the edges with a combination of VitrebondTM, Crazy-GlueTM, and dental acrylic to cover
830 the exposed skull. Mice recovered for ~ 7 days before imaging experiments.

831

832 **Odor delivery:** Odors were presented using a custom-built odor machine as described
833 elsewhere^{78,102}. Undiluted or oil diluted (1:10 or 1:100) odorants were placed in glass vials and
834 airflow through the vials controlled by solenoid valves. The output odor stream was further mixed
835 with clean air in a 50:1 ratio, then this diluted stream was further mixed with clean air at a 5:1 ratio
836 before being sent through short teflon coated tubing placed in front of the mouse's snout. The 12
837 vials in the machine were split into three banks of four vials. Each bank could be independently
838 switched between sending odorized air and clean air to the mouse, in principle allowing
839 combinations of up to three odors. For assessing the effect of modulating GABA-ergic/DAT+
840 interneurons onto mitral and tufted cells responses, we used the following odors: isoamyl acetate,

841 acetaldehyde, valeraldehyde, allyl tiglate, ethyl heptanoate, heptanal, hexanol, 2-hexanone, ethyl
842 tiglate, 1,4 cineole, acetophenone.

843

844 **Data pre-processing**

845 **Movement correction and ROI selection:** Rigid registration in Fiji/ImageJ (template matching)
846 was applied to the acquired fluorescence time-lapse stacks. Images were visually inspected to
847 select a motion-free sequence of frames and create a mean reference image to which we registered
848 each image stack corresponding to a given trial. ROI selection was performed manually (ImageJ):
849 we used both the average and standard deviation projections of the registered images to draw ROIs
850 around the glomeruli and respectively mitral and tufted cell bodies in the FOV.

851

852 **Bleaching correction:** Post ROI extraction (glomeruli, mitral/tufted cells), we applied
853 fluorescence bleaching correction, assuming that: (1) bleaching follows a first order exponential
854 decay across trials for each individual ROI; (2) during the baseline period, any measured activity
855 is random. Given these assumptions, by averaging the fluorescence traces across trials of an ROI,
856 the only robust trend potentially present in the baseline is the characteristic bleaching for that ROI.
857 We checked that the baseline fluorescence of a given ROI is comparable across trials within a
858 session. The procedure used for each ROI was as follows: (1) we fitted an exponential decay
859 function to the fluorescence traces of individual trials, (2) subtracted the fitted function from the
860 ROI trace, (3) averaged the fluorescence traces across all trials for that ROI (aligned to stimulus
861 presentation).

862

863 **Normalization:** For each ROI and trial, we normalized the traces individually, using a
864 fluorescence baseline period (average of ten frames just before the stimulus onset as baseline
865 fluorescence, F_0). For each time point, fractional changes over the baseline fluorescence for the
866 average trace were calculated as dF/F_0 .

867

868 **ROI responsiveness and classification:** On average, stimuli were presented across 4-5 repeats
869 when imaging glomerular responses to optogenetic stimulation, and across 6-10 repeats when
870 sampling the responses of mitral and tufted cells. To evaluate the responsiveness of each
871 glomerulus, we obtained a distribution of average dF/F_0 values from baseline periods, and used
872 95 percentile value of the distribution as response (significant signal) threshold. The baseline
873 reference distribution was obtained from averaging dF/F_0 values quantified over 10-frames
874 intervals extracted from the baseline period and accumulated across all trials. For each ROI, we
875 also obtained peak dF/F_0 values during the optogenetic stimulation frames (1-2 frames). For each
876 ROI, we compared the average response across trials with the baseline reference distribution. If
877 this value crossed the 95th percentile of the baseline distribution, the ROI was classified as
878 responsive (*enhanced*).

879 To evaluate the responsiveness of each mitral and tufted cell, we searched for the peak of a
880 monotonous response (signal) within 5 frames following optogenetic stimulation onset. Similarly,
881 we obtained a distribution of average dF/F_0 values from baseline periods using 4 frames just before
882 the stimulation and accumulating across all trials. We compared the peak response value to the
883 standard deviation (SD) of the baseline. For calling *enhanced* responses, we used 4 SD of the
884 baseline as response (significant signal) threshold; for calling *suppressed* responses, we used 3 SD
885 of the baseline as response threshold to account for the intrinsic lower range of negative deflections

886 from baseline. Cells that had slow and prolonged negative slope ($<15^\circ$) with respect to baseline
887 were not included in further analyses. To assess response reproducibility across trials, for each
888 optogenetic stimulation mask, for each trial, we built a *trial response vector* (using 5-frames from
889 the stimulus onset) and computed the Pearson correlation with respect to the response vectors of
890 the other trials. If for a given trial the average correlation with respect to the response vectors of
891 the other trials, the trial was rejected. For an ROI to be considered for further analysis, at least 2
892 repeats had to pass the criterion. Cells that had slow responses, which occurred only after offset of
893 light stimulation were not included for further analysis to minimize the contribution of
894 disinhibitory effects across the bulb network.

895

896 **Self-response correlations:** To obtain a measure of reliability for ensemble mitral cell responses
897 across different trials to the same DAT+ glomerular photo-stimulation mask, and respectively to
898 the same odorant, using bootstrapping (50 times) in each iteration split the trials into two random
899 subsets of trials, and calculated ‘self’ response correlations, whose average values were $0.81 \pm$
900 0.14 for light masks and 0.87 ± 0.10 for odor responses of the same MC ensembles (**Fig. S5b**).

901

902 For each mitral and tufted cells, the *odor responses* (**Fig. 6**) were calculated as described above
903 using 10-frames periods to build a distribution of baseline values and accumulating across trials.
904 We also used 10-frames periods starting from stimulus onset to search for the response peak. To
905 calculate the *light modulation of the odor response* to DAT+ glomerular photo-stimulation masks
906 (**Figs. 6f-h, S7**), we used as reference the frame just before light stimulation onset. We asked
907 whether in the 2 frames following light onset, we could identify a significant increase/dip in signal
908 compared to this reference dF/F value. A change in signal (defined delta between reference and

909 signal during light stimulation) was considered significant if it amounted to more than 10% of the
910 average peak odor response amplitude (preceding light onset), and was also larger than 3 SDs of
911 the baseline fluorescence (preceding odor onset). To assess response reproducibility across trials,
912 for each stimulus, we performed correlation analysis across trials as described above.

913

914 **Assessing glomerular response spatial extent and specificity:** In Fig. S3c *i* (Right), for each
915 photo-stimulation mask, we normalized the sum total area of the significantly responsive
916 glomerular pixels. We multiplied the sum total area of these responsive pixels by the ratio between
917 the area of the photo-stimulation mask and the surface area of target glomerulus surface. We
918 defined the anatomical outline of each glomerulus in the field of view manually using its baseline
919 fluorescence. To determine the specificity of glomerular responses across light intensities we
920 computed two metrics. First (blue trace, Fig. 4f), we normalized responsive pixels within the
921 boundaries of the target glomerulus by all responsive pixels located within the boundaries of any
922 glomeruli across the FOV. Second (red trace, Fig. 4f), we normalized the significantly responsive
923 pixels within the target glomerulus by the sum area of all responsive pixels within the FOV,
924 including those spanning the juxtglomerular space, surrounding the glomeruli.

925

926 **Correlation analysis and shuffled controls:** For each pairwise correlation analysis (Figs. 6e,h,
927 S5b, S7e-f), we ran 15 repetitions of the shuffling controls and compared the experimental data
928 with the shuffled data (Wilcoxon signed-rank test).

929

930 **Statistical tests:** Depending on the properties of the analyzed data, different statistical tests were
931 used to evaluate the differences between data groups. The information for each statistical

932 comparison is detailed in the legends of each figure panel. ‘Two-sample unpaired Student’s t-test’
933 was used to evaluate significant differences in the means of two normally distributed data sets.
934 ‘The normality of the data distribution was checked using a ‘One-sample Kolmogorov-Smirnov
935 test’ for each data group before the testing differences with the ‘Student’s t-test’. A two-tailed 95%
936 confidence interval was used for both Student’s t-test. Significant differences between two non-
937 normally distributed data sets were evaluated with a nonparametric ‘Wilcoxon signed-rank test.’
938 The linear correlation between two data sets was assessed by computing the Pearson correlation
939 coefficient. When needed, the coefficient of determination (R^2) was used to evaluate how well the
940 compared data sets fit a linear regression model. All the statistical comparisons were tested using
941 MATLAB® using the following functions for each test: ‘Two-sample unpaired Student’s t-test’:
942 ttest; ‘One-sample Kolmogorov-Smirnov test’: kstest; ‘Multiple comparisons of means test’:
943 multcompare; ‘Two-sample Kolmogorov-Smirnov test’: kstest2; ‘Pearson correlation coefficient’:
944 corrccoef. ‘Wilcoxon signed-Rank’: signrank.

References

1. Scanziani, M. & Häusser, M. Electrophysiology in the age of light. *Nature* **461**, 930–939 (2009).
2. Emiliani, V., Cohen, A. E., Deisseroth, K. & Häusser, M. All-Optical Interrogation of Neural Circuits. *J. Neurosci.* **35**, 13917–13926 (2015).
3. Peron, S. & Svoboda, K. From cudgel to scalpel: toward precise neural control with optogenetics. *Nat. Methods* **8**, 30–34 (2011).
4. Prakash, R. *et al.* Two-photon optogenetic toolbox for fast inhibition, excitation and bistable modulation. *Nat. Methods* **9**, 1171–1179 (2012).
5. Adesnik, H. & Abdeladim, L. Probing neural codes with two-photon holographic optogenetics. *Nat. Neurosci.* **24**, 1356–1366 (2021).
6. Lutz, C. *et al.* Holographic photolysis of caged neurotransmitters. *Nat. Methods* **5**, 821–827 (2008).
7. Nikolenko, V. *et al.* SLM Microscopy: Scanless Two-Photon Imaging and Photostimulation with Spatial Light Modulators. *Front. Neural Circuits* **2**, 5 (2008).
8. Packer, A. M. *et al.* Two-photon optogenetics of dendritic spines and neural circuits. *Nat. Methods* **9**, 1202–1205 (2012).
9. Packer, A. M., Russell, L. E., Dagleish, H. W. P. & Häusser, M. Simultaneous all-optical manipulation and recording of neural circuit activity with cellular resolution in vivo. *Nat. Methods* **12**, 140–146 (2015).
10. Carrillo-Reid, L., Yang, W., Bando, Y., Peterka, D. S. & Yuste, R. Imprinting and recalling cortical ensembles. *Science* **353**, 691–694 (2016).
11. Yang, W., Carrillo-Reid, L., Bando, Y., Peterka, D. S. & Yuste, R. Simultaneous two-photon imaging and two-photon optogenetics of cortical circuits in three dimensions. *eLife* **7**, e32671 (2018).
12. Papagiakoumou, E. *et al.* Scanless two-photon excitation of channelrhodopsin-2. *Nat. Methods* **7**, 848–854 (2010).
13. Papagiakoumou, E., Ronzitti, E. & Emiliani, V. Scanless two-photon excitation with temporal focusing. *Nat. Methods* **17**, 571–581 (2020).
14. Villette, V. *et al.* Ultrafast Two-Photon Imaging of a High-Gain Voltage Indicator in Awake Behaving Mice. *Cell* **179**, 1590-1608.e23 (2019).
15. Fan, L. Z. *et al.* All-optical physiology resolves a synaptic basis for behavioral timescale plasticity. *Cell* **186**, 543-559.e19 (2023).
16. Anselmi, F., Ventalon, C., Bègue, A., Ogden, D. & Emiliani, V. Three-dimensional imaging and photostimulation by remote-focusing and holographic light patterning. *Proc. Natl. Acad. Sci. U. S. A.* **108**, 19504–19509 (2011).
17. Anselmi, F., Banerjee, A. & Albeanu, D. F. Patterned Photostimulation in the Brain. in *New Techniques in Systems Neuroscience* (ed. Douglass, A. D.) 235–270 (Springer International Publishing, Cham, 2015).
18. Andrasfalvy, B. K., Zemelman, B. V., Tang, J. & Vaziri, A. Two-photon single-cell optogenetic control of neuronal activity by sculpted light. *Proc. Natl. Acad. Sci. U. S. A.* **107**, 11981–11986 (2010).
19. Rickgauer, J. P., Deisseroth, K. & Tank, D. W. Simultaneous cellular-resolution optical perturbation and imaging of place cell firing fields. *Nat. Neurosci.* **17**, 1816–1824 (2014).
20. Grewe, B. F., Voigt, F. F., van 't Hoff, M. & Helmchen, F. Fast two-layer two-photon imaging of neuronal cell populations using an electrically tunable lens. *Biomed. Opt. Express* **2**, 2035–2046 (2011).
21. Sheffield, M. E. J. & Dombeck, D. A. Calcium transient prevalence across the dendritic arbour predicts place field properties. *Nature* **517**, 200–204 (2015).
22. Iwai, D., Izawa, H., Kashima, K., Ueda, T. & Sato, K. Speeded-Up Focus Control of Electrically Tunable Lens by Sparse Optimization. *Sci. Rep.* **9**, 12365 (2019).

23. Katona, G. *et al.* Fast two-photon in vivo imaging with three-dimensional random-access scanning in large tissue volumes. *Nat. Methods* **9**, 201–208 (2012).
24. Iyer, V., Losavio, B. E. & Saggau, P. Compensation of spatial and temporal dispersion for acousto-optic multiphoton laser-scanning microscopy. *J. Biomed. Opt.* **8**, 460 (2003).
25. Duemani Reddy, G., Kelleher, K., Fink, R. & Saggau, P. Three-dimensional random access multiphoton microscopy for functional imaging of neuronal activity. *Nat. Neurosci.* **11**, 713–720 (2008).
26. Salomé, R. *et al.* Ultrafast random-access scanning in two-photon microscopy using acousto-optic deflectors. *J. Neurosci. Methods* **154**, 161–174 (2006).
27. Akemann, W. *et al.* Fast optical recording of neuronal activity by three-dimensional custom-access serial holography. *Nat. Methods* **19**, 100–110 (2022).
28. Hernandez, O., Pietrajtis, K., Mathieu, B. & Dieudonné, S. Optogenetic stimulation of complex spatio-temporal activity patterns by acousto-optic light steering probes cerebellar granular layer integrative properties. *Sci. Rep.* **8**, 13768 (2018).
29. Hernandez, O. *et al.* Three-dimensional spatiotemporal focusing of holographic patterns. *Nat. Commun.* **7**, 11928 (2016).
30. Oron, D., Papagiakoumou, E., Anselmi, F. & Emiliani, V. Two-photon optogenetics. *Prog. Brain Res.* **196**, 119–143 (2012).
31. Russell, L. E. *et al.* All-optical interrogation of neural circuits in behaving mice. *Nat. Protoc.* **17**, 1579–1620 (2022).
32. Ronzitti, E., Emiliani, V. & Papagiakoumou, E. Methods for Three-Dimensional All-Optical Manipulation of Neural Circuits. *Front. Cell. Neurosci.* **12**, 469 (2018).
33. Pégard, N. C. *et al.* Three-dimensional scanless holographic optogenetics with temporal focusing (3D-SHOT). *Nat. Commun.* **8**, 1228 (2017).
34. Petreanu, L., Huber, D., Sobczyk, A. & Svoboda, K. Channelrhodopsin-2–assisted circuit mapping of long-range callosal projections. *Nat. Neurosci.* **10**, 663–668 (2007).
35. Katz, L. C. & Dalva, M. B. Scanning laser photostimulation: a new approach for analyzing brain circuits. *J. Neurosci. Methods* **54**, 205–218 (1994).
36. Dhawale, A. K., Hagiwara, A., Bhalla, U. S., Murthy, V. N. & Albeanu, D. F. Non-redundant odor coding by sister mitral cells revealed by light addressable glomeruli in the mouse. *Nat Neurosci* **13**, 1404–1412 (2010).
37. Chong, E. *et al.* Manipulating synthetic optogenetic odors reveals the coding logic of olfactory perception. *Science* **368**, (2020).
38. Guo, Z. V., Hart, A. C. & Ramanathan, S. Optical interrogation of neural circuits in *Caenorhabditis elegans*. *Nat. Methods* **6**, 891–896 (2009).
39. Blumhagen, F. *et al.* Neuronal filtering of multiplexed odour representations. *Nature* **479**, 493–498 (2011).
40. Zhu, P., Fajardo, O., Shum, J., Zhang Schäerer, Y.-P. & Friedrich, R. W. High-resolution optical control of spatiotemporal neuronal activity patterns in zebrafish using a digital micromirror device. *Nat. Protoc.* **7**, 1410–1425 (2012).
41. Wyart, C. *et al.* Optogenetic dissection of a behavioural module in the vertebrate spinal cord. *Nature* **461**, 407–410 (2009).
42. Zhu, P., Frank, T. & Friedrich, R. W. Equalization of odor representations by a network of electrically coupled inhibitory interneurons. *Nat. Neurosci.* **16**, 1678–1686 (2013).
43. Banerjee, A. *et al.* An Interglomerular Circuit Gates Glomerular Output and Implements Gain Control in the Mouse Olfactory Bulb. *Neuron* **87**, 193–207 (2015).
44. Leifer, A. M., Fang-Yen, C., Gershow, M., Alkema, M. J. & Samuel, A. D. T. Optogenetic manipulation of neural activity in freely moving *Caenorhabditis elegans*. *Nat. Methods* **8**, 147–152 (2011).

45. Arrenberg, A. B., Stainier, D. Y. R., Baier, H. & Huisken, J. Optogenetic control of cardiac function. *Science* **330**, 971–974 (2010).
46. Farah, N., Reutsky, I. & Shoham, S. Patterned optical activation of retinal ganglion cells. *Conf. Proc. Annu. Int. Conf. IEEE Eng. Med. Biol. Soc. IEEE Eng. Med. Biol. Soc. Conf.* **2007**, 6368–6370 (2007).
47. Fast and light-efficient remote focusing for volumetric voltage imaging | Nature Communications. <https://www.nature.com/articles/s41467-024-53685-5#Bib1>.
48. Botcherby, E. J., Juškaitis, R., Booth, M. J. & Wilson, T. An optical technique for remote focusing in microscopy. *Opt. Commun.* **281**, 880–887 (2008).
49. Botcherby, E. J. *et al.* Aberration-free three-dimensional multiphoton imaging of neuronal activity at kHz rates. *Proc. Natl. Acad. Sci. U. S. A.* **109**, 2919–2924 (2012).
50. Rapid 3D light-sheet microscopy with a tunable lens. <https://opg.optica.org/oe/fulltext.cfm?uri=oe-21-18-21010&id=260811>.
51. Shain, W. J., Vickers, N. A., Goldberg, B. B., Bifano, T. & Mertz, J. Extended depth-of-field microscopy with a high-speed deformable mirror. *Opt. Lett.* **42**, 995–998 (2017).
52. Remote z-scanning with a macroscopic voice coil motor for fast 3D multiphoton laser scanning microscopy. <https://opg.optica.org/boe/fulltext.cfm?uri=boe-7-5-1656&id=338741>.
53. Shepherd, G. M. Synaptic organization of the mammalian olfactory bulb. *Physiol. Rev.* **52**, 864–917 (1972).
54. Wilson, R. I. & Mainen, Z. F. Early events in olfactory processing. *Annu. Rev. Neurosci.* **29**, 163–201 (2006).
55. Arneodo, E. M. *et al.* Stimulus dependent diversity and stereotypy in the output of an olfactory functional unit. *Nat. Commun.* **9**, 1347 (2018).
56. Kikuta, S., Fletcher, M. L., Homma, R., Yamasoba, T. & Nagayama, S. Odorant response properties of individual neurons in an olfactory glomerular module. *Neuron* **77**, 1122–1135 (2013).
57. Padmanabhan, K. & Urban, N. N. Intrinsic biophysical diversity decorrelates neuronal firing while increasing information content. *Nat. Neurosci.* **13**, 1276–1282 (2010).
58. Schwarz, D. *et al.* Architecture of a mammalian glomerular domain revealed by novel volume electroporation using nanoengineered microelectrodes. *Nat. Commun.* **9**, 1–14 (2018).
59. Odour responses of sister projection neurons in the mouse olfactory bulb, revealed by correlative two-photon imaging and synchrotron X-ray holographic nano-tomography. <https://www.abstractsonline.com/pp8/#!/10892/presentation/40650>.
60. Functional interactions between olfactory circuits shapes the timing and structure of odor representations. <https://www.abstractsonline.com/pp8/#!/10892/presentation/40671>.
61. Tootoonian, S., Schaefer, A. T. & Latham, P. E. Sparse connectivity for MAP inference in linear models using sister mitral cells. *PLoS Comput. Biol.* **18**, e1009808 (2022).
62. Aungst, J. L. *et al.* Centre-surround inhibition among olfactory bulb glomeruli. *Nature* **426**, 623–629 (2003).
63. Zavitz, D., Youngstrom, I. A., Borisyuk, A. & Wachowiak, M. Effect of Interglomerular Inhibitory Networks on Olfactory Bulb Odor Representations. *J. Neurosci. Off. J. Soc. Neurosci.* **40**, 5954–5969 (2020).
64. Olsen, S. R., Bhandawat, V. & Wilson, R. I. Divisive normalization in olfactory population codes. *Neuron* **66**, 287–299 (2010).
65. Cleland, T. A. Early transformations in odor representation. *Trends Neurosci.* **33**, 130–139 (2010).
66. Lyons-Warren, A. M. *et al.* Co-transmitting interneurons in the mouse olfactory bulb regulate olfactory detection and discrimination. *Cell Rep.* **42**, 113471 (2023).
67. Papagiakoumou, E., de Sars, V., Oron, D. & Emiliani, V. Patterned two-photon illumination by spatiotemporal shaping of ultrashort pulses. *Opt. Express* **16**, 22039–22047 (2008).

68. Bègue, A. *et al.* Two-photon excitation in scattering media by spatiotemporally shaped beams and their application in optogenetic stimulation. *Biomed. Opt. Express* **4**, 2869–2879 (2013).
69. Papagiakoumou, E. *et al.* Functional patterned multiphoton excitation deep inside scattering tissue. *Nat. Photonics* **7**, 274–278 (2013).
70. Fukunaga, I., Berning, M., Kollo, M., Schmaltz, A. & Schaefer, A. T. Two distinct channels of olfactory bulb output. *Neuron* **75**, 320–329 (2012).
71. Hooks, B. M., Lin, J. Y., Guo, C. & Svoboda, K. Dual-Channel Circuit Mapping Reveals Sensorimotor Convergence in the Primary Motor Cortex. *J. Neurosci.* **35**, 4418–4426 (2015).
72. Chen, T.-W. *et al.* Ultrasensitive fluorescent proteins for imaging neuronal activity. *Nature* **499**, 295–300 (2013).
73. Dana, H. *et al.* Thy1 transgenic mice expressing the red fluorescent calcium indicator jRGECO1a for neuronal population imaging in vivo. *PLoS One* **13**, e0205444 (2018).
74. Mombaerts, P. Axonal wiring in the mouse olfactory system. *Annu. Rev. Cell Dev. Biol.* **22**, 713–737 (2006).
75. Buonviso, N. & Chaput, M. A. Response similarity to odors in olfactory bulb output cells presumed to be connected to the same glomerulus: electrophysiological study using simultaneous single-unit recordings. *J. Neurophysiol.* **63**, 447–454 (1990).
76. Chae, H. *et al.* Mosaic representations of odors in the input and output layers of the mouse olfactory bulb. *Nat. Neurosci.* **22**, 1306–1317 (2019).
77. Fantana, A. L., Soucy, E. R. & Meister, M. Rat olfactory bulb mitral cells receive sparse glomerular inputs. *Neuron* **59**, 802–814 (2008).
78. Gupta, P., Albeanu, D. F. & Bhalla, U. S. Olfactory bulb coding of odors, mixtures and sniffs is a linear sum of odor time profiles. *Nat. Neurosci.* **18**, 272–281 (2015).
79. Adrian, E. D. Olfactory reactions in the brain of the hedgehog. *J. Physiol.* **100**, 459–473 (1942).
80. Niessing, J. & Friedrich, R. W. Olfactory pattern classification by discrete neuronal network states. *Nature* **465**, 47–52 (2010).
81. Wanner, A. A. & Friedrich, R. W. Whitening of odor representations by the wiring diagram of the olfactory bulb. *Nat. Neurosci.* **23**, 433–442 (2020).
82. Boyden, E. S., Zhang, F., Bamberg, E., Nagel, G. & Deisseroth, K. Millisecond-timescale, genetically targeted optical control of neural activity. *Nat Neurosci* **8**, 1263–1268 (2005).
83. Tian, L. *et al.* Imaging neural activity in worms, flies and mice with improved GCaMP calcium indicators. *Nat Meth* **6**, 875–881 (2009).
84. Chan, K. Y. *et al.* Engineered AAVs for efficient noninvasive gene delivery to the central and peripheral nervous systems. *Nat. Neurosci.* **20**, 1172–1179 (2017).
85. Klapoetke, N. C. *et al.* Independent optical excitation of distinct neural populations. *Nat. Methods* **11**, 338–346 (2014).
86. Kebuschull, J. M. *et al.* High-Throughput Mapping of Single-Neuron Projections by Sequencing of Barcoded RNA. *Neuron* **91**, 975–987 (2016).
87. Chen, Y. *et al.* High-throughput sequencing of single neuron projections reveals spatial organization in the olfactory cortex. *Cell* **185**, 4117–4134.e28 (2022).
88. Petersen, C. C. H. Sensorimotor processing in the rodent barrel cortex. *Nat. Rev. Neurosci.* **20**, 533–546 (2019).
89. Han, Y. *et al.* The logic of single-cell projections from visual cortex. *Nature* **556**, 51–56 (2018).
90. Glickfeld, L. L., Andermann, M. L., Bonin, V. & Reid, R. C. Cortico-cortical projections in mouse visual cortex are functionally target specific. *Nat. Neurosci.* **16**, 219–226 (2013).
91. Orsolich, I., Rio, M., Mrcic-Flogel, T. D. & Znamenskiy, P. Mesoscale cortical dynamics reflect the interaction of sensory evidence and temporal expectation during perceptual decision-making. *Neuron* **109**, 1861–1875.e10 (2021).

92. Leinweber, M., Ward, D. R., Sobczak, J. M., Attinger, A. & Keller, G. B. A Sensorimotor Circuit in Mouse Cortex for Visual Flow Predictions. *Neuron* **96**, 1204 (2017).
93. Attinger, A., Wang, B. & Keller, G. B. Visuomotor Coupling Shapes the Functional Development of Mouse Visual Cortex. *Cell* **169**, 1291-1302.e14 (2017).
94. Schneider, D. M., Nelson, A. & Mooney, R. A synaptic and circuit basis for corollary discharge in the auditory cortex. *Nature* **513**, 189–194 (2014).
95. Schneider, D. M., Sundararajan, J. & Mooney, R. A cortical filter that learns to suppress the acoustic consequences of movement. *Nature* **561**, 391–395 (2018).
96. Campbell, R. A. A., Eifert, R. W. & Turner, G. C. Openstage: a low-cost motorized microscope stage with sub-micron positioning accuracy. *PloS One* **9**, e88977 (2014).
97. (PDF) Principles, Design, and Construction of a Two-Photon Laser Scanning Microscope for In Vitro and In Vivo Brain Imaging.
https://www.researchgate.net/publication/233870537_Principles_Design_and_Construction_of_a_Two-Photon_Laser_Scanning_Microscope_for_In_Vitro_and_In_Vivo_Brain_Imaging.
98. Yardeni, T., Eckhaus, M., Morris, H. D., Huizing, M. & Hoogstraten-Miller, S. Retro-orbital injections in mice. *Lab Anim.* **40**, 155–160 (2011).
99. Challis, R. C. *et al.* Systemic AAV vectors for widespread and targeted gene delivery in rodents. *Nat. Protoc.* **14**, 379–414 (2019).
100. Otazu, G. H., Chae, H., Davis, M. B. & Albeanu, D. F. Cortical Feedback Decorrelates Olfactory Bulb Output in Awake Mice. *Neuron* **86**, 1461–1477 (2015).
101. Chae, H., Banerjee, A., Dussauze, M. & Albeanu, D. F. Long-range functional loops in the mouse olfactory system and their roles in computing odor identity. *Neuron* **0**, (2022).
102. Gupta, P., Albeanu, D. F. & Bhalla, U. S. An odor delivery system for arbitrary time-varying patterns of odors, mixtures and concentrations. *bioRxiv* 077875 (2016) doi:10.1101/077875.